Research Square

Preprints are preliminary reports that have not undergone peer review.
They should not be considered conclusive, used to inform clinical practice,
or referenced by the media as validated information.

Mitochondrial iron routing through mitoferrin-1 as a determinant of ferroptotic vulnerability to clinically used iron formulations in ovarian cancer

Anna Martina Battaglia

am.battaglia@unicz.it

Magna Graecia University of Catanzaro https://orcid.org/0000-0003-1976-613X

Emanuele Giorgio

Magna Graecia University of Catanzaro

Giorgia Federico

University of Naples "Federico II"

Sebastiano Vaccarella

IRCCS REGINA ELENA CANCER INSTITUTE https://orcid.org/0009-0005-1937-4699

Sara Donzelli

Regina Elena Cancer Institute https://orcid.org/0000-0002-8529-2895

Giuseppe Natali

Magna Graecia University of Catanzaro

Cristiana Galeano

Magna Graecia University of Catanzaro

Lavinia Petriaggi

Magna Graecia University of Catanzaro

Sandra Mota

University of Coimbra

Claudia De Vitis

Sapienza University of Rome

Nicola Amodio

University Magna Graecia of Catanzaro, Italy

Paulo Oliveira

University of Coimbra

Rita Mancini

Sapienza University of Rome https://orcid.org/0000-0002-5491-2449

Francesco Costanzo

Università Magna Graecia di Catanzaro

Francesca Carlomagno

https://orcid.org/0000-0002-1483-4677

Giovanni Blandino

IRCCS Regina Elena Cancer Institute, Italy https://orcid.org/0000-0002-6970-2241

Flavia Biamonte

Magna Graecia University https://orcid.org/0000-0003-3248-3863

Article

Keywords:

Posted Date: September 14th, 2026

DOI: https://doi.org/10.21203/rs.3.rs-10907717/v1

License: This work is licensed under a Creative Commons Attribution 4.0 International License.
Read Full License

Additional Declarations: (Not answered)

Mitochondrial iron routing through mitoferrin-1 as a determinant of ferroptotic vulnerability to clinically used iron formulations in ovarian cancer

Running title: Mitochondrial iron and ovarian cancer ferroptosis

Emanuele Giorgio[1*], Anna Martina Battaglia[1*§], Giorgia Federico[2], Sebastiano Vaccarella[3], Sara Donzelli[3], Giuseppe Natali[4], Cristiana Galeano[1], Lavinia Petriaggi[1], Sandra Isabel Mota[5,6], Claudia De Vitis[7], Nicola Amodio[1], Paulo Jorge Oliveira[5,6], Rita Mancini[7,8], Francesco Saverio Costanzo[1], Francesca Carlomagno[2], Giovanni Blandino[9] & Flavia Biamonte[1]

[1]Department of Experimental and Clinical Medicine, Magna Graecia University of Catanzaro, Catanzaro, Italy

[2]Department of Molecular Medicine and Medical Biotechnology, University of Naples "Federico II", Naples, Italy

[3]Translational Oncology Research Unit, IRCCS Regina Elena National Cancer Institute, Rome, Italy

[4]Department of Health Sciences, Magna Graecia University of Catanzaro, Catanzaro, Italy

[5]CNC-UC, Center for Neuroscience and Cell Biology, University of Coimbra, Portugal

[6]CiBB - Centre for Innovative Biomedicine and Biotechnology, University of Coimbra, Portugal

[7]Department of Clinical and Molecular Medicine, Sant'Andrea Hospital-Sapienza University of Rome, Rome, Italy

[8]Scuola Superiore di Studi Avanzati Sapienza (SSAS), Sapienza University of Rome, Rome, Italy

[9]Scientific Director's Office, IRCCS Regina Elena National Cancer Institute, Rome, Italy

[*] These authors contributed equally to this work as co-first authors

[§] Corresponding author

am.battaglia@unicz.it

Abstract

Ovarian carcinoma (OVCA) is the most lethal gynaecological malignancy, and platinum resistance sustains its mortality, creating a need for cytotoxic strategies that act independently of apoptosis. OVCA is characterized by an "iron-addicted" phenotype that can render it susceptible to ferroptosis; however, this vulnerability has been tested almost exclusively with non-clinical GPX4/system Xc^- inhibitors, and the determinants of intrinsic sensitivity remain undefined. Here, we tested parenteral iron formulations already in clinical use, namely ferric gluconate, ferric ammonium citrate and iron dextran, as ferroptosis inducers across the PEA1, COV362, KURAMOCHI, and PEO1 OVCA lines. Iron loading killed PEA1 and COV362 through ferroptosis, rescued by ferrostatin-1 but not by inhibitors of apoptosis, necroptosis or autophagy, and accompanied by lipid peroxidation, cytoplasmic reactive oxygen species (ROS) and GPX4 loss, while sparing non-malignant ovarian epithelial cells; sensitivity was independent of both canonical GPX4/system Xc^- inhibition and platinum-response status. Mechanistically, the resistant PEO1 and KURAMOCHI cells mounted the canonical protective response to iron overload, by restricting import through transferrin-receptor (TfR1) downregulation, enhancing iron export via ferroportin upregulation, and promoting mitochondria clearance through PARKIN-mediated mitophagy. In contrast, the sensitive PEA1 and COV362 cells failed to activate those mechanisms and instead preferentially directed iron to the mitochondria via mitoferrin-1 (MFRN1), resulting in mitochondrial ROS accumulation and bioenergetic failure. Silencing MFRN1 protected sensitive cells and abolished mitochondrial iron loading without lowering the cytosolic iron pool, identifying the mitochondrial iron pool as the lethal determinant. *In vivo*, iron dextran suppressed the growth of sensitive but not resistant cells-derived xenografts, with induction of ferroptosis markers (*PTGS2*, *MFRN1*) and *GPX4* downregulation, and no caspase activation. Overall, we identified mitochondrial iron routing through MFRN1 as determinant of ferroptotic vulnerability in OVCA and propose repurposed iron formulations as a therapeutic strategy for a molecularly defined subset of this disease.

Introduction

Ovarian carcinoma (OVCA) remains the most lethal gynaecological malignancy, and despite initial responsiveness to platinum-based chemotherapy the emergence of platinum resistance accounts for most treatment failures [1,2]. Strategies that engage cell-death programmes distinct from apoptotic machinery predominantly exploited by conventional cytotoxic agents are therefore of particular interest.

Ferroptosis, the iron-dependent, non-apoptotic cell death driven by the accumulation of lipid hydroperoxides beyond the detoxifying capacity of the GPX4 antioxidant system [3–8], represents one such vulnerability, and OVCA appears intrinsically prone to this process. When compared to the normal epithelium, OVCA exhibits reduced ferroportin (FPN)-mediated efflux and increased transferrin-receptor (TfR1)-mediated import that together drive intracellular iron accumulation and an acquired dependence on iron for proliferation [9–11]. Hence, this "iron-addicted" state has been proposed as a therapeutic liability [9,12]. Two questions remain unresolved. First, can iron itself, delivered through parenteral iron formulations already in routine clinical use, function as a *bona fide* ferroptosis inducer (FIN) in OVCA? Such a mechanism would represent a class-IV, iron-overload mode of ferroptosis induction and offer an immediately repositionable strategy. Second, and more fundamentally, why are iron-addicted OVCA cells not uniformly sensitive to ferroptosis? Even within the same histological subtype, some tumors succumb to iron overload whereas others tolerate a comparable iron burden[13]. We reasoned that the critical determinant is not the magnitude of iron uptake but rather its intracellular handling, specifically whether labile iron pool (LIP) is safely buffered and exported or instead directed to mitochondria, where it can initiate the lipid peroxidation cascade that drives ferroptotic cell death. So far, whether mitochondria are required for ferroptosis has remained controversial, as their contribution appears to depend on the initiating trigger [3,14]; in the specific setting of iron overload-driven death, the role of mitochondrial iron import, and particularly of its carrier mitoferrin-1 (MFRN1), has not been defined.

Here, using a panel of four OVCA lines, we show that clinically used iron formulations (ferric gluconate, ferric ammonium citrate, iron dextran) induce ferroptosis and reveal a striking sensitive/resistant dichotomy. Notably, this response is independent of platinum sensitivity status and does not correlate with susceptibility to class-I and class-II FINs, namely system Xc^- and GPX4 inhibitors. We traced this dichotomy to divergent iron handling: sensitive cells fail to mount the protective import-down/export-up response and instead channel iron into the mitochondrion via MFRN1, generating mitochondrial ROS, bioenergetic failure and GPX4 loss. In contrast, resistant cells restrict iron uptake, enhance export and storage, and actively remodel their mitochondrial network through fission and mitophagy to mitigate the effects of iron overload. Silencing *MFRN1* protects sensitive cells from ferroptosis despite continued accumulation of cytosolic iron, identifying the mitochondrial iron pool as the lethal determinant. In accordance, iron supply *in vivo* selectively reduces growth of sensitive, but not resistant cells. These findings identify mitochondrial iron routing as the critical determinant of ferroptosis susceptibility in OVCA and identify clinically available iron formulations as a potential therapeutic strategy for a defined and targetable subset of OVCA.

Results

Clinically used iron formulations induce ferroptosis in a defined subset of OVCA cells

To test whether iron can act as a FIN, we incubated four OVCA cell lines (PEA1, COV362, KURAMOCHI, PEO1) and one immortalised human ovarian surface epithelium cell line (IHOSE) to two chemically distinct, clinically used iron formulations, sodium ferric gluconate (ferlixit) and ferric ammonium citrate (FAC), over a 0-500μM range for 24h. The cytotoxic dose-dependently effect of both compounds on cell viability was strongly evident for PEA1, representing the most sensitive cell line, with cell death reaching ≈70% at 500μM ferlixit, and significant loss (≈30% cell death) already at 100μM. COV362 showed an intermediate response (≈40% at 500μM; ≈20% at 100μM) while KURAMOCHI, PEO1 and the non-malignant IHOSE were not affected at any doses (viability>85%). FAC reproduced the same hierarchy with lower potency (Fig. 1A-B). Iron-induced cell death by

ferlixit (100μM) and FAC (100μM) treatments (≈40% PI^+ cells in PEA1, ≈29% in COV362) was rescued only by the ferroptosis inhibitor ferrostatin-1 (Fer-1, 50μM), and not by the pan-caspase inhibitor Z-VAD-FMK (Z-VAD, 20μM), by the necroptosis inhibitor necrostatin-1 (Necr-1, 10μM), or by the autophagy inhibitor bafilomycin A1 (Baf, 1μM), identifying ferroptosis as the main cell-death mechanism (Fig. 1C). Consistently, iron loading induced the ferroptosis-selective membrane-ballooning morphology selectively in PEA1 and COV362, but not in the resistant lines or in IHOSE (Fig. 1D). Intracellular ROS (including hydroxyl radical, hydrogen peroxide and hypochlorite anion) rose markedly after ferlixit or FAC in PEA1 and COV362, but not in KURAMOCHI, PEO1 or IHOSE cells (Fig. 2A). Lipid peroxidation, measured by using BODIPY-C11, mirrored this pattern: the oxidized dye MFI increased to 36.7 (ferlixit) and 13.9 (FAC) in PEA1, and to 20.1 (ferlixit) and 8.12 (FAC) in COV362, while remaining negligible in KURAMOCHI, PEO1, and IHOSE (Fig. 2B). Upon iron treatment the ferroptosis gatekeeper GPX4 was downregulated in the sensitive PEA1 and COV362, but significantly upregulated in the resistant KURAMOCHI and PEO1, while unchanged in IHOSE (Fig. 2C). Finally, we treated all four cell lines with the canonical class-2 (RSL3) and class-1 (erastin2) FINs (Fig. S1A, B) and found that sensitivity to iron was uncoupled from sensitivity to either agent. Notably, the iron-resistant KURAMOCHI cells were highly sensitive to GPX4 inhibition, reaching up to 90.2% PI^+ cells at 10μM RSL3, indicating a fully competent ferroptotic execution machinery. Conversely, the iron-sensitive PEA1 cells were largely refractory to system Xc^- inhibition, exhibiting only ≈12% PI^+ at 10μM erastin2. This vulnerability signature was also independent from platinum-response status: reported cisplatin IC_{50} indicate that the iron-sensitive PEA1 are less sensitive to platinum than the iron-resistant PEO1 cells [15], and the iron-sensitive COV362 is among the most platinum-resistant lines [16], demonstrating that susceptibility to iron-induced ferroptosis does not simply reflect sensitivity to conventional platinum-based chemotherapy.

Resistant OVCA cells activate the canonical protective response to iron overload, whereas sensitive OVCA cells retain iron

Next, we investigated how the two groups of cell lines handled iron loading. Live-cell imaging of the LIP using FerroOrange revealed that, in the sensitive PEA1 and COV362 cells, treatment with ferlixit and FAC induced a marked FerroOrange signal already a T0, a timepoint that includes the probe incubation time, compared with untreated T0. This indicates that iron uptake begins essentially as soon as the cells are exposed to the two compounds. The signal then reached a pronounced Fe^{2+} peak at 1h which subsequently declined by 12-24h. In contrast, the resistant KURAMOCHI and PEO1 cells showed no detectable increase in the LIP, with fluorescence profiles remaining indistinguishable from those of untreated controls at all time points (Fig. 3A). Iron loading failed to alter surface expression of the iron importer TfR1 in PEA1 and COV362 cells at 24h, whereas it induced a significant downregulation of TfR1 in the resistant KURAMOCHI and PEO1 cells (Fig. 3B). The sole known iron exporter FPN was downregulated in the sensitive PEA1 and COV362 cells at 24h, whereas its expression increased in the resistant KURAMOCHI and PEO1 for the same time point. Ferritin heavy chain 1 (FtH1) was upregulated in all four cell lines at 24h, indicating that increased iron storage is a shared response to iron loading, and does not discriminate between iron-sensitive and iron-resistant phenotypes (Fig. 3C). Together, these results indicate that the resistant cell lines mounted the canonical adaptative response to iron overload by restricting iron uptake, enhancing iron export, and increasing iron storage. In contrast, the sensitive cell lines failed to engage this protective program, maintaining TfR1 expression while suppressing iron export.

Mitochondrial iron trafficking and remodelling dictate ferroptotic vulnerability in OVCA cells

Then, we explored whether the iron retained in sensitive OVCA cells was trafficked to specific organelles, in particular mitochondria. Flow-cytometric quantification of mitochondrial ferrous iron using Mito-FerroGreen revealed a rapid accumulation of mitochondrial Fe^{2+} in the sensitive PEA1 cells following ferlixit exposure, with the proportion of Mito-FerroGreen-positive cells increasing from 13.4% to 37.5% within 1h before returning to baseline levels by 24h. A similar, albeit less pronounced, response was observed in COV362 cells, in which Mito-FerroGreen positivity increased

from 3.54% to 11.1% at 1h. KURAMOCHI cells, instead, reduced mitochondrial iron levels following treatment with the proportion of Mito-FerroGreen-positive cells decreasing from 27.6% to 8.87% at 1h. In PEO1 cells, mitochondrial iron remained consistently low throughout the experiment, with fewer than 3% of cells staining positive at any time point (Fig. 4A). Western blot analysis showed that the mitochondrial iron importer MFRN1 was upregulated in PEA1 cells, remained unchanged in COV362 cells, and was downregulated in both KURAMOCHI and PEO1 cells (Fig. 4B). Mitochondrial superoxide ($O_2^{\bullet -}$), measured using MitoSOX, increased selectively in the sensitive PEA1 and COV362 cells, while remaining unchanged in KURAMOCHI and PEO1 cells (Fig. 4C). This was accompanied by mitochondrial dysfunction in the highly sensitive PEA1 cells, which exhibited increased proton leak and reduced spare respiratory capacity, indicative of mitochondrial uncoupling and impaired respiratory function. In contrast, the resistant cell lines were largely spared, with PEO1 cells showing only a modest reduction in non-mitochondrial respiration (Fig. 4D; full OCR and ECAR profiles, as well as energetic map shown in Fig. S2A-C). Notably, upon iron loading, resistant PEO1 cells showed an upregulation of the fission effectors DRP1 and MFF together with the mitophagy marker PARKIN (Fig. 4E); this response in PEO1 resistant cells was supported by a reduction in mitochondrial mass, as measured by MitoTracker Green (Fig. S2D), consistent with the selective elimination of iron-stressed mitochondria through mitochondrial quality-control mechanisms. KURAMOCHI cells showed an upregulation of the fission marker DRP1, without a significant change in MFF or PARKIN, suggesting engagement of a fission-related mitochondrial response rather than direct evidence of active fission (Fig. 4E).

MFRN1 knockdown-mediated mitochondrial iron restriction counteracts ferroptosis sensitivity in PEA1 cells

To determine the contribution of cytosolic and mitochondrial iron import to iron-induced ferroptosis, we inhibited TfR1-mediated cytosolic iron uptake using the TfR1-blocking peptide (iTfR1) and blocked mitochondrial iron import using pooled siRNA-mediated silencing of *MFRN1*

in the most sensitive PEA1 cells (knockdown efficiency shown in Fig. S3). Ferlixit-induced cell death (≈44.8% PI^+ in the control situation) was significantly reduced by *MFRN1* silencing, decreasing to 19.2% and providing greater protection than TfR1 blockade, which reduced cell death to 29.0%. A similar hierarchy was observed following FAC treatment, with cell death decreasing from 27.9% PI^+ cells in control cultures to 6.9% following MFRN1 silencing and to 14.3% following TfR1 blockade (Fig. 5A). Combining the two interventions did not produce an additive effect (siMFRN1 + iTfR1, 26.9% upon ferlixit and 11.8% FAC), suggesting that TfR1-mediated iron uptake and MFRN-1-dependent mitochondrial iron import operate within the same linear pathway rather through independent mechanisms. Based on previous time-course experiments with ferlixit and FAC, the effects of iTfR1 and siMFRN1 silencing on iron distribution were assessed at 1h, corresponding to the peak of both cytosolic and mitochondrial iron accumulation, rather than at 24h, when iron levels had largely returned close to baseline. Importantly, neither intervention substantially altered the cytosolic LIP as FerroOrange MFI remained comparable across control, iTfR1-treated, siMFRN1 and combination-treatment conditions, suggesting that protection from death was not attributable to a reduction in total cytosolic iron (Fig. 5B). TfR1 blockade produced a slight reduction in treatment-induced mitochondrial iron with Mito-FerroGreen positivity decreasing from 38.1% in ferlixit-treated control PEA1 cells to 30.7%. In contrast, *MFRN1* silencing largely abolished mitochondrial iron accumulation, returning Mito-FerroGreen levels to those observed in untreated PEA1 cells (≈10-17%). Combined inhibition did not further reduce mitochondrial iron beyond the effect achieved by *MFRN1* silencing alone (21.5%), further suggesting a model in which TfR1-mediated iron uptake and MFRN1-dependent mitochondrial import operate along a common linear pathway rather than as additive, independent routes (Fig. 5C).

Iron delivery induces ferroptosis and suppresses growth in PEA1- but not PEO1-derived xenografts

Because iron dextran (FeDex) is the iron formulation most used in *in vivo* studies due to its well characterized parenteral pharmacokinetics and tolerability, we selected it for evaluation in PEA1 and PEO1 cell line-derived xenograft (CDX) models. Prior to *in vivo* testing, we first confirmed that FeDex recapitulated the sensitivity hierarchy observed *in vitro* (Fig. 6; Fig. S4A). SCID mice were injected subcutaneously with PEA1 or PEO1 cells. Once tumors became palpable, mice were randomized to receive FeDex (80mg/kg) or vehicle twice weekly, and tumor growth was monitored over a two-week treatment period (Fig. 6A). FeDex significantly suppressed the growth of the sensitive PEA1-derived xenografts, reducing tumor volume by ≈65% at day 19 ($p<0.001$) and by ≈50% at day 23 ($p<0.01$). In contrast, FeDex had no detectable effect on the growth of the resistant PEO1 tumors (Fig. 6B), thereby recapitulating the *in vitro* sensitivity dichotomy in an *in vivo* setting. The growth-inhibitory effect of FeDex in PEA1 was accompanied by a significant reduction in the proliferation marker phospho-histone H3 ($PH3^+$ cells/field, $p<0.001$), whereas PH3 expression remained unchanged in PEO1 tumors (Fig. 6C). In contrast, cleaved caspase-3 levels were unaffected in both models (Fig. 6D), arguing against apoptosis being the primary mechanism of tumor-cell death. To confirm that the observed growth suppression was associated with ferroptosis, we analysed the expression of ferroptosis- associated and iron metabolism- related transcripts in the xenograft tumors (Fig. 6E). In PEA1-derived xenografts, FeDex treatment induced the ferroptosis marker prostaglandin-endoperoxide synthase 2 (*PTGS2)*, as well as *MFRN1,* while significantly reducing *GPX4* and *FPN* expression ($p<0.01$). In contrast, this transcriptional program was largely absent in the resistant PEO1 tumors where *PTGS2, GPX4*, *MFRN1, FPN* and *TfR1* expression were unchanged, consistent with iron exposure in the absence of ferroptotic commitment (Fig. 6E). Finally, the analysis of the systemic pharmacological effect of the treatment (Fig. S4B, C) demonstrated that FeDex markedly increased hepatic iron content, serum iron levels, and transferrin saturation in both PEA1- and PEO1-bearing mice. These findings confirm that the divergent tumor responses were not derived from differences in systemic iron loading, comparable in the two models.

Discussion

Our study establishes that susceptibility to iron-induced ferroptosis in OVCA is determined not by the amount of iron acquired by the cell but by its intracellular fate. This reframes the "iron-addicted" phenotype in OVCA [9,10,17]: an avid iron economy is shared by OVCA cells but becomes lethal only in those that channel labile iron into mitochondria. We identify MFRN1 as a central regulator of this process and demonstrate that parenteral iron formulations already approved for clinical use can exploit this vulnerability. In doing so, our findings extend previous work showing that iron administration can overcome ferroptosis resistance in OVCA [13], repositioning iron from a sensitizer of canonical FINs to a stand-alone therapeutic strategy with a defined mechanistic basis. Although ferroptosis is repeatedly proposed to circumvent platinum resistance in OVCA [17–21], the vulnerability has been explored almost exclusively with the non-clinical tool compounds erastin and RSL3, with natural products with limited translational development [22], or in combination with PARP inhibitors [23]. By showing that ferric gluconate, ferric ammonium citrate and iron dextran act as *bona fide* FINs, we extend the class-IV, iron-oxidation mode of induction, so far represented only by FINO2, and recently reviewed by us OVCA [12,24], to a set of clinically approved iron formulations.

The central role of mitochondria in this form of cell death is still under debate: based on the current literature, ferroptosis can proceed without a functional electron transport chain [3], yet mitochondria are required for cysteine-deprivation-, but not for GPX4-inhibition-induced ferroptosis [6,14,25]. Our present data place iron-overload ferroptosis within the mitochondria-dependent category. Silencing *MFRN1* protected cells from ferroptosis death while leaving the cytosolic LIP unchanged, thereby formally dissociating the mitochondrial iron pool from total cellular iron as the critical lethal compartment. These findings are consistent with the emerging gatekeeper role of mitochondrial iron transporters, including MFRN1/2, VDAC2/3 or MCU [25,26]. Our findings are also consistent with the only previous study implicating MFRN1 in cancer ferroptosis, conducted in hepatocellular carcinoma (HCC), where ENO1-mediated suppression of IRP1 reduced MFRN1 expression and limited mitochondrial iron-dependent ferroptosis[27].

Resistant OVCA cells mounted the canonical adaptative response to iron characterized by reduced TfR1-mediated iron uptake, enhanced FPN-dependent iron export, increased FtH1 expression, preservation or reinforcement of GPX4 expression, and the clearance of iron-laden mitochondria through mitochondrial fission and PARKIN-dependent mitophagy. In contrast, sensitive cells failed to engage this protective program. Recent studies suggest that mitophagy and ferritinophagy can amplify ferroptosis by releasing iron and ROS from damaged mitochondria [28]. Conversely, disruption of mitochondrial dynamics has been reported to attenuate ferroptosis through activation of the AMPK-NRF2-FSP1 protective axis [25,29]. In this regard, our data distinguish mitochondrial fission from productive mitophagic clearance: DRP1 alone was insufficient to confer protection against iron overload, as it occurred in PEA1 cells and KURAMOCHI cells without concomitant PARKIN induction. By contrast, only PEO1 resistant cell line activated a coordinated DRP1/MFF-PARKIN program accompanied by loss of mitochondrial. Collectively, these findings indicate that the complete fragmentation-and-removal response, rather than mitochondrial fission per se, protects cells from ferroptosis. This upstream resistance mechanism, which operates through the regulation of intracellular iron trafficking is mechanistically distinct, yet complementary, from the downstream NRF2/FSP1/GPX4 antioxidant defences that are most implicated in ferroptosis resistance in OVCA [30,31]. Importantly, our iron-loading resistant OVCA models retained a fully competent ferroptotic execution machinery, as exemplified by KURAMOCHI cells, which were resistant to iron-induced ferroptosis, yet among the most sensitive to GPX4 inhibitor RSL3. This places the resistance mechanism at the level of iron handling and delivery rather than at the terminal lipid peroxidation step. Consistent with this interpretation, sensitivity to iron overload correlated with neither erastin nor RSL3 responsiveness and was dissociated from platinum sensitivity. Indeed, COV362, one of the most platinum-resistant OVCA cell lines [15], was highly sensitive to iron-induced ferroptosis, whereas platinum-sensitive PEO1 cells displayed marked resistance to iron. This orthogonality may reveal a therapeutically exploitable vulnerability within the platinum-refractory disease that drives OVCA mortality, consistent with the principle that therapy-resistant persister cells

acquire a heightened dependence on mitochondrial ROS and increase susceptibility to ferroptosis[32,33]. The *in vivo* findings strengthen the translational relevance of these results. FeDex, a parenteral iron formulation with established clinical use, produced pronounced and selective suppression of ferroptosis-sensitive PEA1 xenografts while leaving resistant PEO1 tumors entirely unaffected, despite comparable systemic iron loading in both models. This dissociation excludes differential drug exposure or bioavailability as a confounding explanation and instead pinpoints a cell-autonomous determinant of iron-induced ferroptotic vulnerability, intrinsic to the tumor rather than to the treatment. The antitumor response was accompanied by reduced proliferation without a concomitant increase in cleaved caspase-3, arguing against apoptosis as the operative cell-death pathway. Instead, the induction of PTGS2 and MFRN1, alongside GPX4 downregulation and reduced FPN expression, provides a coherent molecular signature of ferroptotic commitment, one that faithfully recapitulates the MFRN1-dependent iron-routing phenotype we defined *in vitro*. These data move beyond correlative evidence to establish proof of concept that pharmacological iron delivery can achieve a robust, mechanism-consistent antitumor effect in vivo, and they provide a strong rationale for evaluating FeDex in biomarker-selected OVCA populations.

Overall, in this study we identify mitochondrial iron routing through MFRN1 as a determinant of ferroptotic vulnerability in OVCA and show that clinically available iron formulations can exploit it to kill a defined, platinum-independent subset of tumors. Future work should establish the sufficiency of the MFRN1 axis, dissect its interplay with NRF2/FSP1, and validate baseline iron-handling markers as response predictors in patient-derived models. Positioning iron not as a nutrient to be withheld but as a cytotoxic agent to be delivered offers a conceptually distinct with potential translational relevance in a disease with urgent need of new options.

Materials and Methods

Cell lines and cell culture

Human ovarian cancer cell lines PEA1, COV362, and PEO1 (ECACC, Sigma-Aldrich, St. Louis, MO, United States) and KURAMOCHI (JCRB, Osaka, Japan) were used, together with the normal ovarian surface epithelial line IHOSE (Applied Biological Materials, Richmond, BC, Canada). PEA1 and PEO1 were cultured in RPMI 1640, COV362 in DMEM (all Sigma-Aldrich, St. Louis, MO, United States), and KURAMOCHI in RPMI 1640 with 20% FBS; IHOSE cells were grown in PriGrow IV medium (abm Inc., Richmond, BC, Canada). All media were supplemented with 10% (v/v) FBS (Invitrogen, San Diego, CA, United States), unless otherwise specified, and 1% (v/v) penicillin/streptomycin (Sigma-Aldrich, St. Louis, MO, United States). Cells were maintained at 37°C, 5% CO_2, routinely tested for mycoplasma contamination, and authenticated by STR profiling.

Reagents

Ferlixit (62.5mg/5ml, sodium ferric gluconate complex in sucrose; Sanofi, Paris, France) was obtained from the outpatient pharmacy of "Magna Graecia" University of Catanzaro. FAC (F5879), Fer-1 (SML0583), zVAD (V116), Baf (B1793), Necr-1 (480065), erastin2 (SML2794) and FeDex (D8517) were purchased from Sigma-Aldrich (St. Louis, MO, United States); RSL3 (HY-100218A) from MedChemExpress (MCE, Monmouth Junction, NJ, United States); and iTfR1 (ab101219) from Abcam (Cambridge, United Kingdom). FeDex was selected as the iron source for in vivo experiments based on its tolerability for parenteral administration, whereas in vitro treatments required millimolar concentrations. Dose-response experiments (24h) used the following concentrations: ferlixit and FAC at 25, 50, 100, 250, and 500µM; RSL3 and erastin2 at 2, 5, and 10µM; FeDex at 5 and 25mM (in vitro) and 80mg/kg (in vivo); Fer-1 at 50µM; zVAD at 20µM; Baf at 1µM; Necr-1 at 10µM; iTfR1 at 20µg/ml for 6h. Ferlixit and FAC were used at 100µM in all subsequent experiments.

Propidium iodide staining

Single-cell suspensions were stained with propidium iodide (PI, Thermo Fisher Scientific, Waltham, MA, United States) at 37°C for 15min in the dark, washed twice with PBS, and analysed by flow

cytometry (BD LSRFortessa™ X-20; BD Biosciences, San Jose, CA, United States) [34]. For each condition, 2×10^4 events were collected and analysed using FlowJo™ v10 software (BD Biosciences, San Jose, CA, United States).

Live/Dead cell viability assay

Cell viability was assessed using the Live/Dead Cell Viability Assay Kit (Merck Millipore, Burlington, MA, United States). Cells were seeded in 96-well plates (3×10^3 cells/well), treated as indicated, and incubated with the Live/Dead staining solution at 37°C for 30min in the dark. Fluorescence was acquired on an Opera Phenix Plus high-throughput confocal imager (Revvity, Waltham, MA, United States), and live/dead cells were quantified using Harmony High-Content Imaging and Analysis Software (Revvity, Waltham, MA, United States).

Optical microscopy of the "ballooning" phenotype

Cells were seeded in 96-well plates (3×10^3 cells/well) and allowed to adhere overnight. After treatment, morphological changes corresponding to the "ballooning" phenotype were assessed by phase-contrast light microscopy (Leica DM IL LED inverted microscope; Leica Microsystems, Wetzlar, Germany).

Intracellular ROS detection assay

Intracellular ROS levels were assessed using PhenoVue™ ROS 670 reagent (Revvity, Waltham, MA, United States). Cells were seeded in 96-well plates (3×10^3 cells/well), treated as indicated, and incubated with the dye at 37°C for 30min in the dark. Images were acquired on an Opera Phenix Plus imager (Revvity, Waltham, MA, United States) and quantified using Harmony software (Revvity, Waltham, MA, United States).

Lipid peroxidation analysis

Lipid peroxidation was assessed by flow cytometry using BODIPY™ 581/591 C11 (Thermo Fisher Scientific, Waltham, MA, United States). Cells were incubated with 2.5µM dye at 37°C for 30min, washed twice with PBS (1X); oxidation was detected as a fluorescence emission shift from ~590nm to ~510nm, proportional to lipid peroxidation. Acquisition was performed on a BD LSRFortessa™ X-20 flow cytometer (BD Biosciences, San Jose, CA, United States), with $\geq 2\times10^4$ cells analysed per condition using FlowJo™ v10 software (BD Biosciences, San Jose, CA, United States).

Labile iron pool (LIP) analysis

Intracellular LIP was assessed using FerroOrange (Cell Signaling Technology, Danvers, MA, United States), a Fe^{2+}-selective dye. Cells were incubated with 1µmol/l FerroOrange for 30min at 37°C in the dark and analysed by flow cytometry and live-cell imaging. For flow cytometry, cells were washed with PBS (1X) and acquired on a BD LSRFortessa™ X-20 flow cytometer (BD Biosciences, San Jose, CA, United States); fluorescence was quantified using FlowJo™ v10 software (BD Biosciences, San Jose, CA, United States). For live-cell imaging, fluorescence was acquired on a Leica THUNDER Imaging System DMi8 (Leica Microsystems S.r.l., Wetzlar, Germany).

Surface TfR1 analysis

Surface TfR1 expression was analysed by flow cytometry. Cells were incubated with anti-human TfR1-PE antibody (Miltenyi Biotec, Bergisch Gladbach, Germany) for 10min at 4°C in the dark, washed twice with PBS (1X), and acquired on a BD LSRFortessa™ X-20 flow cytometer (BD Biosciences, San Jose, CA, United States); data were analysed using FlowJo™ v10 software (BD Biosciences, San Jose, CA, United States).

Mitochondrial iron detection

Mitochondrial Fe^{2+} was detected using Mito-FerroGreen (Dojindo, Kumamoto, Japan). Cells were fixed and permeabilized with the BD Cytofix/Cytoperm kit (BD Biosciences, San Jose, CA, United

States) and loaded with 5µmol/L Mito-FerroGreen for 30min at 37°C. After two PBS (1X) washes, cells were acquired on a BD LSRFortessa™ X-20 flow cytometer (BD Biosciences, San Jose, CA, United States) and analysed with FlowJo™ v10 software (BD Biosciences, San Jose, CA, United States).

Measurement of mitochondrial superoxide anion

Mitochondrial superoxide was assessed using MitoSOX™ Red (Thermo Fisher Scientific, Waltham, MA, United States). Cells (3×10^3/well, 96-well plates) were treated and incubated with 1µM MitoSOX™ Red in HBSS (Ca^{2+}/Mg^{2+}) for 10min at 37°C in the dark, washed with HBSS, and counterstained with 1µg/ml Hoechst 33342 (Thermo Fisher Scientific, Waltham, MA, United States) for 10min at 37°C in the dark. Fluorescence images were acquired at 20x magnification using a Nikon Eclipse Ti inverted fluorescence microscope (Nikon Instruments Inc., Tokyo, Japan) and analysed using Fiji (ImageJ, National Institutes of Health, Bethesda, MD, United States); superoxide levels were quantified as corrected total cell fluorescence (CTCF).

Total protein extraction and Western blot analysis

Total protein was extracted using RIPA buffer (1M Tris HCl, 3M NaCl, Triton X-100, 10% SDS, 0.5M EDTA) with cOmplete™ Protease Inhibitor Cocktail (Roche Diagnostics, Mannheim, Germany), and lysates were centrifuged (12,000×g, 30min, 4°C) [24,35]. Protein concentration was determined using Bio-Rad Protein Assay Dye (Bio-Rad Laboratories, Hercules, CA, United States). Protein (50µg) was separated on 8-12% SDS-PAGE gels and transferred to nitrocellulose membranes (Sigma-Aldrich, St. Louis, MO, United States), blocked with 5% non-fat milk or BSA, and incubated overnight at 4°C with primary antibodies: GPX4 (1:1000, ab41787), PARKIN (1:1000, ab77924), and FPN (1:500, ab235166) (Abcam, Cambridge, United Kingdom); FtH1 (1:200, sc-376594; Santa Cruz Biotechnology, Dallas, TX, United States); TfR1 (1:1000, #13208), IRP2 (1:1000, #20272), DRP1 (1:1000, #14647), and MFF (1:1000, #84580) (Cell Signaling Technology, Danvers, MA,

United States); and MFRN1 (1:1000, abs1051; Merck Millipore, Burlington, MA, United States). Membranes were incubated with peroxidase-conjugated secondary antibodies (Peroxidase AffiniPure Sheep Anti-Mouse IgG, Donkey Anti-Rabbit IgG, and Donkey Anti-Goat IgG, all 1:10,000; Jackson ImmunoResearch Europe Ltd, Ely, United Kingdom), and signals were visualized by chemiluminescence (ECL Western Blotting Detection System; Santa Cruz Biotechnology, Dallas, TX, United States) and acquired using a Uvitec Alliance Mini HD9 imaging system (Uvitec, Cambridge, United Kingdom). Band intensities were quantified using ImageJ (National Institutes of Health, Bethesda, MD, United States) and normalised to GAPDH-HRP (1:3000, sc-47724) or ɣ-tubulin (sc-177787) (Santa Cruz Biotechnology, Dallas, TX, United States) as loading controls. Full length WB have been uploaded as Supplementary Material.

Seahorse XF analysis

OCR and ECAR were measured on a Seahorse XFe96 analyzer (Agilent Technologies, Santa Clara, CA, United States). Cells (6×10^3/well) were seeded in Seahorse XF96 microplates. Culture medium was replaced with pH 7.4 assay medium matched to each model's growth conditions: DMEM-grown cells received 25mM glucose and 4mM L-glutamine, RPMI-1640-grown cells received 11mM glucose and 2mM L-glutamine (all Thermo Fisher Scientific, Waltham, MA, United States). Plates were equilibrated for 1h at 37°C in a non-CO_2 incubator. Mitochondrial respiration was assessed using the Seahorse XF Cell Mito Stress Test, with sequential injection of oligomycin (Port A), BAM15 (Port B), and rotenone/antimycin A (Port C), each at 2µM. OCR/ECAR values were normalised to protein mass (SRB assay, Sigma-Aldrich, St. Louis, MO, United States) and analysed with Wave v2.3 software (Agilent Technologies, Santa Clara, CA, United States).

Sulforhodamine B (SRB) assay

Protein content was determined using SRB (Sigma-Aldrich, St. Louis, MO, United States). Cells were fixed with 60% trichloroacetic acid (TCA, Sigma-Aldrich, St. Louis, MO, United States) and

incubated at 4°C for protein precipitation. Plates were washed, air-dried, and stained with 0.05% SRB in 1% acetic acid for 30min at room temperature in the dark. Unbound dye was removed with 1% acetic acid washes, and plates were dried at 37°C. Protein-bound SRB was solubilized in 10mM Tris-NaOH buffer (pH 10.5, Sigma-Aldrich, St. Louis, MO, United States), and absorbance was measured at 510nm (background subtraction at 620nm) using a Cytation 3 cell imaging multi-mode reader (BioTek Instruments Inc., Winooski, VT, United States). SRB values were used to normalize Seahorse OCR/ECAR data.

Assessment of mitochondrial content

Mitochondrial content was evaluated using MitoTracker™ Green FM (Thermo Fisher Scientific, Waltham, MA, United States). Cells in 96-well plates were incubated with 200nM MitoTracker™ Green FM in HBSS (Ca^{2+}/Mg^{2+}) for 30min at 37°C in the dark, washed, and counterstained with 1µg/ml Hoechst 33342 (Thermo Fisher Scientific, Waltham, MA, United States) for 10min at 37°C in the dark. Fluorescence images were acquired at 20x magnification using a Nikon Eclipse Ti inverted fluorescence microscope (Nikon Instruments Inc., Tokyo, Japan) and analysed using Fiji (ImageJ, National Institutes of Health, Bethesda, MD, United States); content was quantified as corrected total cell fluorescence (CTCF).

MFRN1 transient knockdown

PEA1 cells (2×10^5/well, 6-well plates) were allowed to adhere overnight to ~70-80% confluence, then transfected with 50nM ON-TARGETplus 2.0 Human SMARTpool SLC25A37 siRNA (L2-007369-01-0050) or ON-TARGETplus Non-targeting Pool (D-001810-10) (Dharmacon, Lafayette, CO, United States) using Lipofectamine™ 3000 Transfection Reagent (Thermo Fisher Scientific, Waltham, MA, United States) in Opti-MEM™ Reduced Serum Medium (Gibco, Thermo Fisher Scientific, Waltham, MA, United States), per manufacturer's instructions. After 6h, transfection

medium was replaced with complete growth medium, and cells were cultured for 48h before downstream analysis. Transfection efficiency was confirmed by qRT-PCR.

RNA isolation and quantitative real-time PCR analysis

Total RNA was isolated using TRIzol™ reagent (Life Technologies, Carlsbad, CA, United States) and treated with DNase (Thermo Fisher Scientific, Waltham, MA, United States); RNA quality/concentration were determined spectrophotometrically [36,37]. cDNA was synthesized from 1µg total RNA using the High-Capacity cDNA Reverse Transcription Kit (Thermo Fisher Scientific, Waltham, MA, United States). qRT-PCR was performed using SYBR™ Green qPCR Master Mix (Thermo Fisher Scientific, Waltham, MA, United States) on a QuantStudio™ 3 Real-Time PCR System (Thermo Fisher Scientific, Waltham, MA, United States). Relative mRNA expression of MFRN1, GPX4, PTGS2, FPN, FtH1, and TfR1 was calculated using the $2^{-}\Delta\Delta CT$ method, with GAPDH as housekeeping gene. Primer sequences are in Table 1.

Table 1: List of primer sequences used for qRT-PCR.

Gene name	Primer forward	Primer reverse
MFRN1	5'-CGGGATAGCTGGGAGTATGG-3'	5'-GTGTAGCTCCGGTAGAAGGC-3'
GPX4	5'-ATCGACGGGCACATGGTTAA-3'	5'-CGACGAGCTGAGTGTAGTTT-3'
PTGS2	5'-CTCCTGTGCCTGATGATTGC-3'	5'-AACTGATGCGTGAAGTGCTG-3'
FPN	5'-TTGCGGTGTCTGTGTTTCTG-3'	5'-AGGTCTGGGCCACTTAAGT-3'
FtH1	5'-CATCAACCGCCAGATCAAC-3'	5'-GATGGCTTTCACCTGCTCA-3'
TfR1	5′-TGCTGCTTTCCCTTTCCTTG-3′	5′-GCTCGTGCCACTTTGTTCAA-3′
GAPDH	5′-CAAATTCCATGGCACCGTCA-3′	5′-GGCAGAGATGATGACCCTTT-3′

***In vivo* tumor xenograft model**

In vivo ferroptosis studies were performed at the Department of Molecular Medicine and Medical Biotechnology, University of Naples Federico II, per Italian animal experimentation regulations

(Italian Ministry of Health Authorization No. 683/2024-PR). Female SCID mice (Charles River Laboratories, Wilmington, MA, United States) were injected subcutaneously under isoflurane anaesthesia into right and left flanks with PEO1 (5×10^6 cells/mouse) or PEA1 (2×10^6 cells/mouse) cells, respectively. After 11 days, when tumors became palpable, mice were randomised to intraperitoneal FeDex or vehicle (1X PBS) twice weekly for 2 weeks. Tumor volume was calculated as $V=A\times B^2/2$ (A: axial diameter, B: rotational diameter). No treatment-related toxicity or wasting was observed. Maximal tumor size permitted (Italian Ministry of Health) was 1500mm²; mice were euthanized by CO_2 inhalation when tumors reached 1000mm². Tumors were snap-frozen in liquid nitrogen or fixed in 10% formalin.

***In vivo* IHC analysis**

FFPE tumor sections (5µm) were deparaffinized, rehydrated (graded xylene/ethanol, 100–50%), and processed for IHC: endogenous peroxidase was blocked with 3% H_2O_2, followed by citrate buffer antigen retrieval. Sections were blocked with 1% BSA for 30min and incubated overnight at 4°C with anti-cleaved Caspase-3 (#9661) or anti-phospho-Histone H3 (PH3, #9701) (Cell Signaling Technology, Danvers, MA, United States). After PBS washes, sections were incubated with biotinylated goat anti-rabbit secondary antibody (30min, room temperature; #BA-1000-1.5, Vector Laboratories, Burlingame, CA, United States), visualized with DAB, and examined on a Leica DMD108 microscope (Leica Microsystems, Wetzlar, Germany).

***In vivo* iron status assessment**

Serum iron and transferrin saturation were measured using a total iron binding capacity kit (TI4064, Randox Laboratories Ltd, Crumlin, United Kingdom), per manufacturer's instructions. For liver iron concentration, liver tissue was dried overnight at 110°C, mechanically dissociated, weighed, and

digested in 1ml of 3M HCl/0.6M TCA overnight at 65°C; total non-heme iron was measured by the bathophenanthroline method.

Statistical analysis

Experiments used ≥3 independent biological replicates. Statistical analyses were performed using GraphPad Prism v10 (GraphPad Software, San Diego, CA, United States). Data are mean ± SD from ≥3 independent biological replicates. Two-group comparisons used two-tailed unpaired Student's t-test; ≥3-group comparisons used one- or two-way ANOVA with appropriate post hoc tests, as indicated in figure legends. $P<0.05$ was considered significant.

References

1 Matulonis UA, Sood AK, Fallowfield L, Howitt BE, Sehouli J, Karlan BY. Ovarian cancer. *Nat Rev Dis Primers* 2016; **2**: 1–22.

2 Scott CL, Banerjee S, Joly F, Lee JM, Mukhopadhyay A, Tan DS *et al.* Ovarian cancer. *Nature Reviews Disease Primers 2026 12:1* 2026; **12**: 10-.

3 Dixon SJ, Lemberg KM, Lamprecht MR, Skouta R, Zaitsev EM, Gleason CE *et al.* Ferroptosis: an iron-dependent form of nonapoptotic cell death. *Cell* 2012; **149**: 1060–1072.

4 Stockwell BR. Ferroptosis turns 10: Emerging mechanisms, physiological functions, and therapeutic applications. *Cell* 2022; **185**: 2401–2421.

5 Yang WS, Sriramaratnam R, Welsch ME, Shimada K, Skouta R, Viswanathan VS *et al.* Regulation of ferroptotic cancer cell death by GPX4. *Cell* 2014; **156**: 317–331.

6 Battaglia AM, Chirillo R, Aversa I, Sacco A, Costanzo F, Biamonte F. Ferroptosis and cancer: Mitochondria meet the “iron maiden” cell death. *Cells* 2020; **9**. doi:10.3390/cells9061505.

7 Giorgio E, Galeano C, Natali G, Petriaggi L, Faniello MC, Janda E *et al.* Interaction of Ferroptosis and Immune-Mediated Inflammation in Psoriasis. *Antioxidants (Basel)* 2026; **15**. doi:10.3390/ANTIOX15030382.

8 Biamonte F, Natali G, Galeano C, Lamanna R, Petriaggi L, Costanzo FS *et al.* The good, the bad, and the iron: Ferroptosis and macrophages in ovarian cancer. *Ferroptosis and Oxidative Stress* 2026; **2**: 202605–202605.

9 Basuli D, Tesfay L, Deng Z, Paul B, Yamamoto Y, Ning G *et al.* Iron addiction: A novel therapeutic target in ovarian cancer. *Oncogene* 2017; **36**: 4089.

10 Torti S V., Torti FM. Iron and cancer: more ore to be mined. *Nat Rev Cancer* 2013; **13**: 342–355.

11 Battaglia AM, Sacco A, Vecchio E, Scicchitano S, Petriaggi L, Giorgio E *et al.* Iron affects the sphere-forming ability of ovarian cancer cells in non-adherent culture conditions. *Front Cell Dev Biol* 2023; **11**. doi:10.3389/FCELL.2023.1272667.

12 Petriaggi L, Giorgio E, Natali G, Galeano C, Furtado SR, Faniello CM *et al.* Iron Fist in a Velvet Glove: Class IV Ferroptosis Inducers as a Novel Strategy to Target Ovarian Cancer. *Front Biosci (Landmark Ed)* 2025; **30**: 39675.

13 Battaglia AM, Sacco A, Perrotta ID, Faniello MC, Scalise M, Torella D *et al.* Iron Administration Overcomes Resistance to Erastin-Mediated Ferroptosis in Ovarian Cancer Cells. *Front Oncol* 2022; **12**. doi:10.3389/fonc.2022.868351.

14 Gao M, Yi J, Zhu J, Minikes AM, Monian P, Thompson CB *et al.* Role of Mitochondria in Ferroptosis. *Mol Cell* 2019; **73**: 354-363.e3.

15 Stukova M, Hall MD, Tsotsoros SD, Madigan JP, Farrell NP, Gottesman MM. Reduced accumulation of platinum drugs is not observed in drug-resistant ovarian cancer cell lines derived from cisplatin-treated patients. *J Inorg Biochem* 2015; **149**: 45.

16 Haley J, Tomar S, Pulliam N, Xiong S, Perkins SM, Karpf AR *et al.* Functional characterization of a panel of high-grade serous ovarian cancer cell lines as representative experimental models of the disease. *Oncotarget* 2016; **7**: 32810–32820.

17 Kapper C, Oppelt P, Arbeithuber B, Gyunesh AA, Vilusic I, Stelzl P *et al.* Targeting ferroptosis in ovarian cancer: Novel strategies to overcome chemotherapy resistance. *Life Sci* 2024; **349**: 122720.

18 Ruan D, Wen J, Fang F, Lei Y, Zhao Z, Miao Y. Ferroptosis in epithelial ovarian cancer: a burgeoning target with extraordinary therapeutic potential. *Cell Death Discovery 2023 9:1* 2023; **9**: 1–10.

19 Li S, Yang L, Zhu Z. Ferroptosis and chemotherapy resistance in ovarian cancer: molecular mechanisms and therapeutic opportunities. *J Ovarian Res* 2026; **19**. doi:10.1186/S13048-026-02150-6.

20 Wu X, Liu Q, Jiang Z, Wang G, Liao L, Ye X *et al.* Targeting ferroptosis: a promising avenue for ovarian cancer treatment. *Front Immunol* 2025; **16**: 1578723.

21 Kobayashi H, Yoshimoto C, Matsubara S, Shigetomi H, Imanaka S. A comprehensive overview of recent developments on the mechanisms and pathways of ferroptosis in cancer: the potential implications for therapeutic strategies in ovarian cancer. *Cancer Drug Resist* 2023; **6**: 547–566.

22 Zhao Y, Lu L, Chen X, Yin Q. Natural compounds targeting ferroptosis in ovarian cancer: Research progress and application potential. *Pharmacol Res* 2025; **215**: 107729.

23 Zhang J, Ouyang D, Liu M, Xiang Y, Li Z. Research progress on ferroptosis and PARP inhibitors in ovarian cancer: action mechanisms and resistance mechanisms. *Front Pharmacol* 2025; **16**: 1598279.

24 Battaglia AM, Sacco A, Giorgio E, Petriaggi L, Elzanowska J, Cruz AR *et al.* Expulsion of iron-rich ferritin via CD63-mediated exosome drives ferroptosis resistance in ovarian cancer cells. *Front Cell Dev Biol* 2025; **13**: 1532097.

25 Liu Y, Lu S, Wu L lei, Yang L, Yang L, Wang J. The diversified role of mitochondria in ferroptosis in cancer. *Cell Death Dis* 2023; **14**. doi:10.1038/S41419-023-06045-Y.

26 Ding Z, Li Z, Sun K, Liu Y, Fang Z, Sun S *et al.* Mitochondrial Regulation of Ferroptosis in Cancer Cells. *Int J Biol Sci* 2025; **21**: 2179–2200.

27 Liao C, He Y, Luo X, Deng G. Ferroptosis: insight into the treatment of hepatocellular carcinoma. *Cancer Cell International 2024 24:1* 2024; **24**: 376-.

28 Yu F, Zhang Q, Liu H, Liu J, Yang S, Luo X *et al.* Dynamic O-GlcNAcylation coordinates ferritinophagy and mitophagy to activate ferroptosis. *Cell Discovery 2022 8:1* 2022; **8**: 40-.

29 Ma S, Qin J, Zhang Y, Luan J, Sun N, Hou G *et al.* Disrupting mitochondrial dynamics attenuates ferroptosis and chemotoxicity via upregulating NRF2-mediated FSP1 expression. *Cell Rep* 2025; **44**. doi:10.1016/j.celrep.2025.116234.

30 Wang N, Chen M, Wu M, Liao Y, Xia Q, Cai Z *et al.* High-adhesion ovarian cancer cell resistance to ferroptosis: The activation of NRF2/FSP1 pathway by junctional adhesion molecule JAM3. *Free Radic Biol Med* 2025; **228**: 1–13.

31 Tahsin T, McPhail DK, Champion JD, Alzahrani MAM, Hilditch ML, Faris-Orr A *et al.* Targeting NRF2 and FSP1 to Overcome Ferroptosis Resistance in TSC2-Deficient and Cancer Cells. *Cancers (Basel)* 2025; **17**. doi:10.3390/CANCERS17162714.

32 Hangauer MJ, Viswanathan VS, Ryan MJ, Bole D, Eaton JK, Matov A *et al.* Drug-tolerant persister cancer cells are vulnerable to GPX4 inhibition. *Nature* 2017; **551**: 247–250.

33 Higuchi M, Williams AF, Stuhlfire AE, Nguyen AH, Gervasio DAG, Turkal CE *et al.* FSP1 and histone deacetylases suppress cancer persister cell ferroptosis. *Sci Adv* 2026; **12**: eaea8771.

34 Sacco A, Battaglia AM, Santamaria G, Buffone C, Barone S, Procopio A *et al.* SOX2 promotes a cancer stem cell-like phenotype and local spreading in oral squamous cell carcinoma. *PLoS One* 2023; **18**. doi:10.1371/JOURNAL.PONE.0293475.

35 Zolea F, Biamonte F, Battaglia AM, Faniello MC, Cuda G, Costanzo F. Caffeine Positively Modulates Ferritin Heavy Chain Expression in H460 Cells: Effects on Cell Proliferation. *PLoS One* 2016; **11**. doi:10.1371/JOURNAL.PONE.0163078.

36 Battaglia AM, Sacco A, Aversa I, Santamaria G, Palmieri C, Botta C *et al.* Iron-mediated oxidative stress induces PD-L1 expression via activation of c-Myc in lung adenocarcinoma. *Front Cell Dev Biol* 2023; **11**: 1208485.

37 Petriaggi L, Giorgio E, Bulotta S, Antonelli A, Bonacci S, Frisina M *et al.* Acute Exposure to Cadmium Triggers NCOA4-Mediated Ferritinophagy and Ferroptosis in Never-Smokers Oral Cancer Cells. *Int J Biol Sci* 2025; **21**: 4131–4152.

38 Chirillo R, Aversa I, Di Vito A, Salatino A, Battaglia AM, Sacco A *et al.* FtH-Mediated ROS Dysregulation Promotes CXCL12/CXCR4 Axis Activation and EMT-Like Trans-Differentiation in Erythroleukemia K562 Cells. *Front Oncol* 2020; **10**: 698.

39 Di Sanzo M, Aversa I, Santamaria G, Gagliardi M, Panebianco M, Biamonte F *et al.* FTH1P3, a Novel H-Ferritin Pseudogene Transcriptionally Active, Is Ubiquitously Expressed and Regulated during Cell Differentiation. *PLoS One* 2016; **11**: e0151359.

Figure Legends

Fig.1 Ferlixit and FAC reduce viability and trigger ferroptosis selectively in PEA1 and COV362 cell lines.

A Viability of PEA1, COV362, KURAMOCHI, PEO1 and IHOSE cells after 24h of ferlixit (top) or FAC (bottom), 25, 50, 100, 250, and 500µM, expressed as percentage of viable (PI^-) cells by flow cytometry. Mean±SD, n=3; one-way ANOVA. Asterisks: versus untreated at each concentration. **B** Representative fluorescence images of the five lines left untreated or treated with 100µM ferlixit or FAC (24h), assessed by Live/Dead Cell Viability assay (Opera Phenix Plus): Hoechst 33342 (blue, nuclei) and propidium iodide (red, dead cells); boxed regions magnified in insets. Scale bars, 200µm. Graphs: PI^+ (dead) nuclei expressed as a fraction of total nuclei and normalised to untreated (RFU), with individual data points shown. Mean ± SD, n=3; one-way ANOVA. **C** PI^+ cells (%) by flow cytometry in the five lines treated with 100µM ferlixit or FAC (24h) alone or in combination with Fer-1 (50µM), Z-VAD (20µM), Necr-1 (10µM) or Baf (1µM). Mean ± SD, n=3; one-way ANOVA. PEA1 and COV362 cell death was rescued by Fer-1 only. **D** Representative phase-contrast images under the same conditions as B. Yellow arrowheads: ballooning morphology; boxed regions magnified in insets. Scale bars, 100 µm. Graphs: ballooned cells (%). Mean ± SD, n=3; one-way ANOVA. *p<0.05, **p<0.01, ***p<0.001, ****p<0.0001; ns, not significant.

Fig. 2 Iron loading induces lipid peroxidation and GPX4 loss in sensitive lines.

A Representative fluorescence images of PEA1, COV362, KURAMOCHI, PEO1 and IHOSE cells left untreated or treated with 100µM ferlixit or FAC (24h), stained with Hoechst 33342 (blue, nuclei) and PhenoVue ROS 670 (red, intracellular ROS); boxed regions magnified in insets. Scale bars, 200µm. Graphs: ROS-associated fluorescence normalised to untreated (RFU), replicates overlaid. Mean ± SD, n=3; one-way ANOVA. **B** Lipid peroxidation assessed by flow cytometry using BODIPY 581/591 C11 in the five cell lines under the same conditions. Representative flow cytometry plots (PE-A versus Alexa Fluor 488-A); numbers indicate the percentage of cells with oxidised dye. Graphs: BODIPY-C11 mean fluorescence intensity (MFI). Mean ± SD, n=3; one-way ANOVA. **C** Representative immunoblots of GPX4 in the five cell lines left untreated or treated with 100µM ferlixit or FAC (24 h), with GAPDH as loading control; densitometry (right) normalised to GAPDH.

Mean ± SD, n=3; one-way ANOVA. *p<0.05, **p<0.01, ***p<0.001, ****p<0.0001; ns, not significant.

Fig. 3 Differential iron handling underlies ferroptosis sensitivity.

A Time-course of the LIP assessed by live-cell imaging with FerroOrange (magenta, Fe^{2+}) in PEA1, COV362, KURAMOCHI and PEO1 cells, left untreated or treated with 100µM ferlixit or FAC, at T0, 1h, 12h and 24h. Scale bars, 100µm. Graphs: FerroOrange fluorescence (RFU) over time. Mean ± SD, n=3; two-way ANOVA (versus untreated at each time point). **B** Surface TfR1 assessed by flow cytometry in the four cell lines left untreated or treated with 100µM ferlixit or FAC (24h). Representative histograms (normalised to mode) with per-condition MFI values indicated; bar graph shows TfR1 MFI. Mean ± SD, n=3; two-way ANOVA. **C** Representative immunoblots of FtH1 and FPN in the four cell lines left untreated or treated with 100µM ferlixit or FAC (24h), with GAPDH as loading control; densitometry (below) normalised to GAPDH. Mean ± SD, n=3; one-way ANOVA. *p<0.05, **p<0.01, ***p<0.001, ****p<0.0001; ns, not significant.

Fig.4 Mitochondrial iron trafficking and remodeling dictate ferroptotic vulnerability.

A Mitochondrial iron assessed by flow cytometry with Mito-FerroGreen in PEA1, COV362, KURAMOCHI and PEO1 cell lines (ferlixit or FAC, 100µM, at 1h and 24h). Representative plots with percentage of Mito-FerroGreen^{+} cells indicated; bar graphs show Mito-FerroGreen MFI. Mean ± SD, n=3; two-way ANOVA. **B** Representative immunoblots of MFRN1 in the four cell lines upon treatment with 100µM ferlixit or FAC (24h), with GAPDH as loading control; densitometry (below) normalised to GAPDH. Mean ± SD, n=3; one-way ANOVA. **C** Mitochondrial superoxide anion assessed by MitoSOX Red (yellow) with Hoechst 33342 (blue, nuclei); representative fluorescence images. Scale bars, 200µm. Graphs: MitoSOX fluorescence normalised to untreated cells, with individual data points shown. Mean ± SD, n=3; one-way ANOVA. **D** Oxygen consumption rate (OCR) parameters - proton leak, spare respiratory capacity and non-mitochondrial respiration - from

the Seahorse XF Cell Mito Stress Test in the four lines untreated or treated with 100μM ferlixit or FAC (24h), normalised to cell protein content by using the SRB assay. Mean ± SD, n=3; two-way ANOVA. **E** Representative immunoblots of PARKIN, MFF and DRP1 in the four lines untreated or treated with 100μM ferlixit or FAC (24h), with GAPDH as loading control; densitometry (below) normalised to GAPDH. Mean ± SD, n=3; one-way ANOVA. *p<0.05, **p<0.01, ***p<0.001, ****p<0.0001; ns, not significant.

Fig. 5 MFRN1-dependent mitochondrial iron import is required for iron-induced ferroptosis.
A PI^+ cells (%) by flow cytometry in PEA1 transfected with control or *MFRN1* siRNA (siMFRN1), with or without iTfR1 (20μg/ml, 6h), and left untreated or treated with 100μM ferlixit or FAC (24h). Representative plots with %PI^+ indicated; bar graph (right). Mean ± SD, n=3; two-way ANOVA. **B** Cytosolic LIP assessed by flow cytometry with FerroOrange in PEA1 under the conditions in A. Representative histograms (normalised to mode) with per-condition MFI indicated; bar graph (right). Mean ± SD, n=3; two-way ANOVA. **C** Mitochondrial iron assessed by flow cytometry with Mito-FerroGreen in PEA1 under the conditions in A. Representative plots with percentage of positive cells indicated; bar graphs (below) show Mito-FerroGreen MFI. Mean ± SD, n=3; one-way ANOVA. *p<0.05, **p<0.01; ns, not significant.

Fig. 6 *In vivo* iron administration suppresses growth and induces ferroptosis only in sensitive xenografts.
A Schematic of the xenograft experiment. PEA1 (2×10^6) or PEO1 cells (5×10^6) were inoculated subcutaneously into SCID mice (day 0); iron dextran (FeDex, 80mg/kg) treatment started on day 11 and was administered intraperitoneally twice a week; tumor volume was monitored twice weekly (days 12-23); animals were sacrificed on day 23. Created with BioRender.com. **B** Growth curves of PEA1 (top) and PEO1 (bottom) cell line-derived xenografts (CDX) in untreated and FeDex-treated

(80mg/kg) mice. Left panels show tumor volume (mm^3) over time (days); right panels show the corresponding distributions at days 19 and 23. Mean ± SD, n=8 tumors per group; two-way ANOVA. **C** Representative IHC for PH3 in PEA1 and PEO1 xenografts, with quantification ($PH3^+$ cells/field). Scale bars, 100µm. Violin plots show all analysed fields (n=10 fields from 3 tumors per group); Student's *t*-test. **D** Representative IHC for cleaved caspase-3 in the same xenografts, with quantification (cleaved $caspase\text{-}3^+$ cells/field). Scale bars, 100µm. Violin plots and statistics as in **C**. **E** qRT-PCR of ferroptosis- and iron-handling related genes (*GPX4*, *PTGS2*, *FPN*, *FtH1*, *MFRN1*, *TfR1*) in PEA1 (top) and PEO1 (bottom) xenografts, expressed as mRNA relative expression (FeDex versus untreated, normalised to GAPDH). Mean ± SD, n=5; two-way ANOVA. *p<0.05, **p<0.01, ***p<0.001; ns, not significant.

Competing interests

The authors declare no competing financial interests.

Data Availability

All data generated or analysed during this study are included in this published article and its supplementary information files.

Acknowledgements

The authors thank the Centre of the Interdepartmental Services (CIS) of Magna Graecia University of Catanzaro (Catanzaro, Italy) for PEA1 and PEO1 cells and Dr Luca Palazzo ("Federico II" University of Naples, Italy) for COV362 and KURAMOCHI cell lines. The authors are grateful to CIS of Magna Graecia University of Catanzaro for providing access to advanced instrumentation, including the live-cell imaging system (Leica Thunder DMi8 microscope) and the flow cytometry platform (BD Fortessa X20).

Funding

This study was supported by funds from the Unione Europea - Next Generation Eu, Missione 4 Componente 1, CUP F53D23003840006. PRIN - Progetti di Ricerca di Interesse Nazionale - Bando 2022 - Prot. 2022R85H27. This work was also co-funded by the EU Recovery and Resilience Facility and Portuguese national funds via FCT – Fundação para a Ciência e a Tecnologia, under projects, LA/P/0058/2020 [DOI: 10.54499/LA/P/0058/2020], UID/PRR/4539/2025 [DOI: 10.54499/UID/PRR/04539/2025] and UID/04539/2025.

Author Contributions

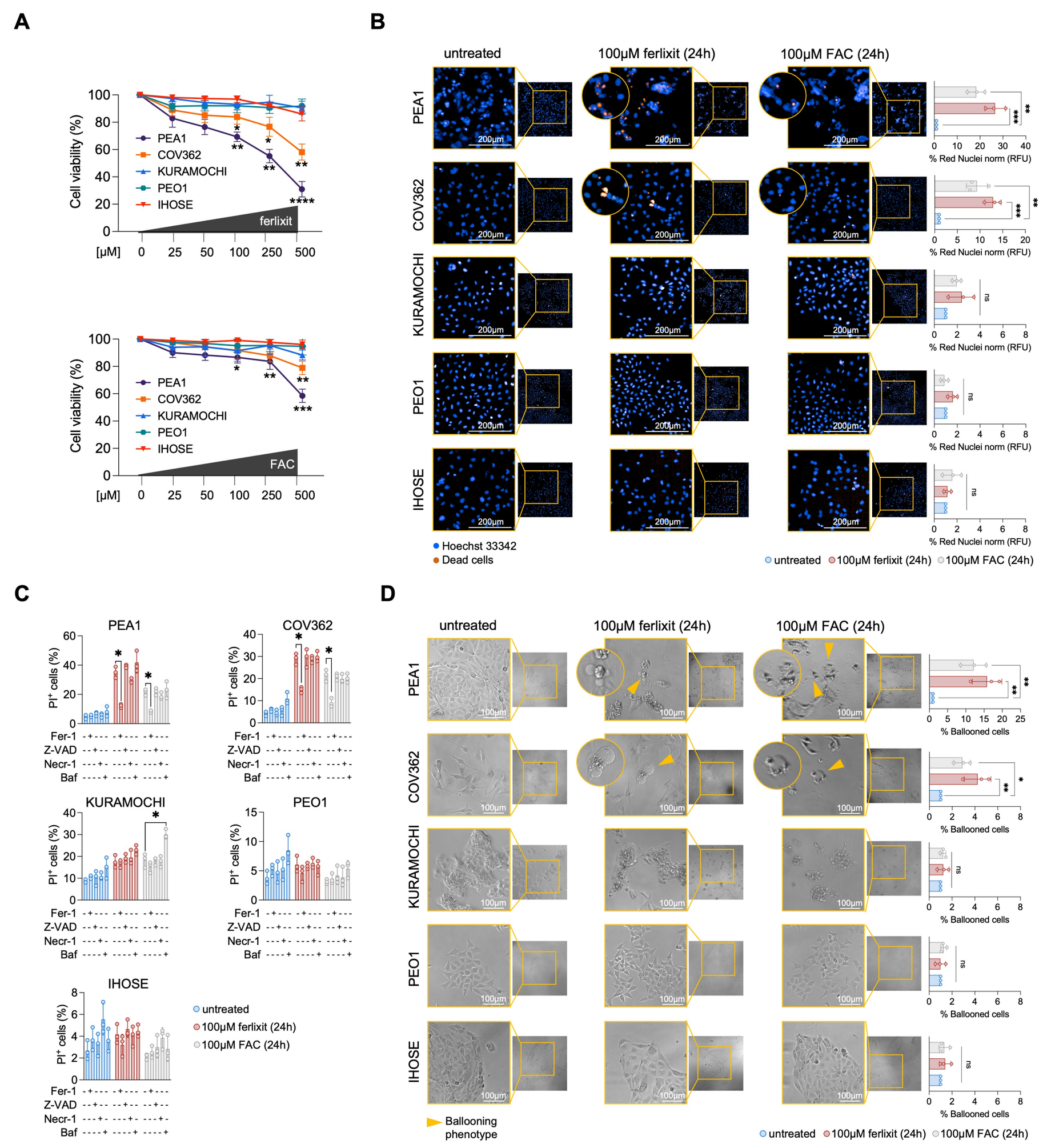
Conceptualization: FB and AMB. Methodology: EG, AMB, GF, SV, SD, GN, CG, LV, SIM, and CDV. Investigation: EG, AMB, GF, SV, SD, GN, CG, LV, SIM, NA and CDV. Writing-Original Draft: EG, AMB and FB. Review and Editing: AMB, PJO, FSC, RM, FC, GB and FB. Funding Acquisition: FB and CDV. Supervision: FB

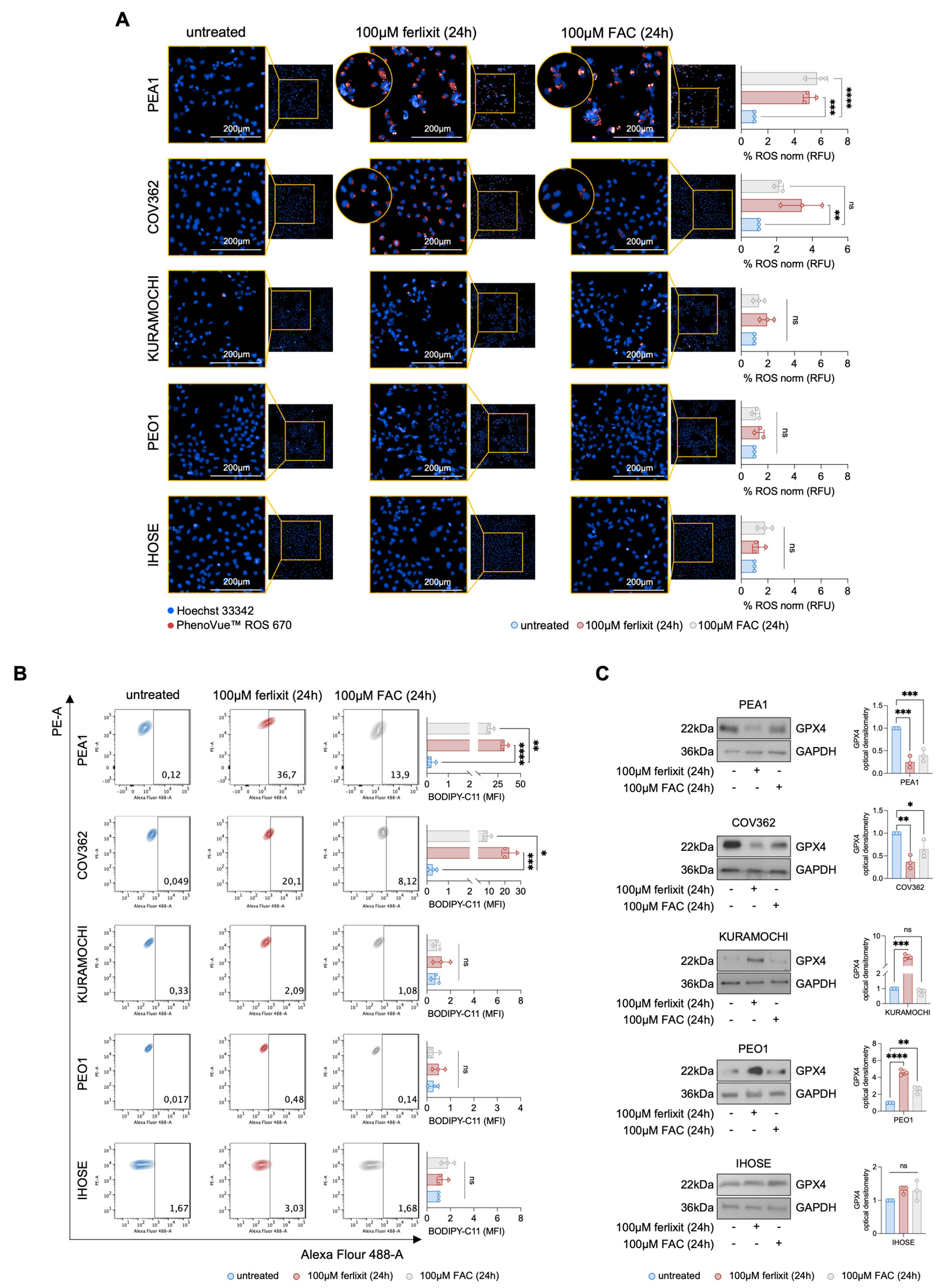
Corresponding author

Correspondence to Anna Martina Battaglia

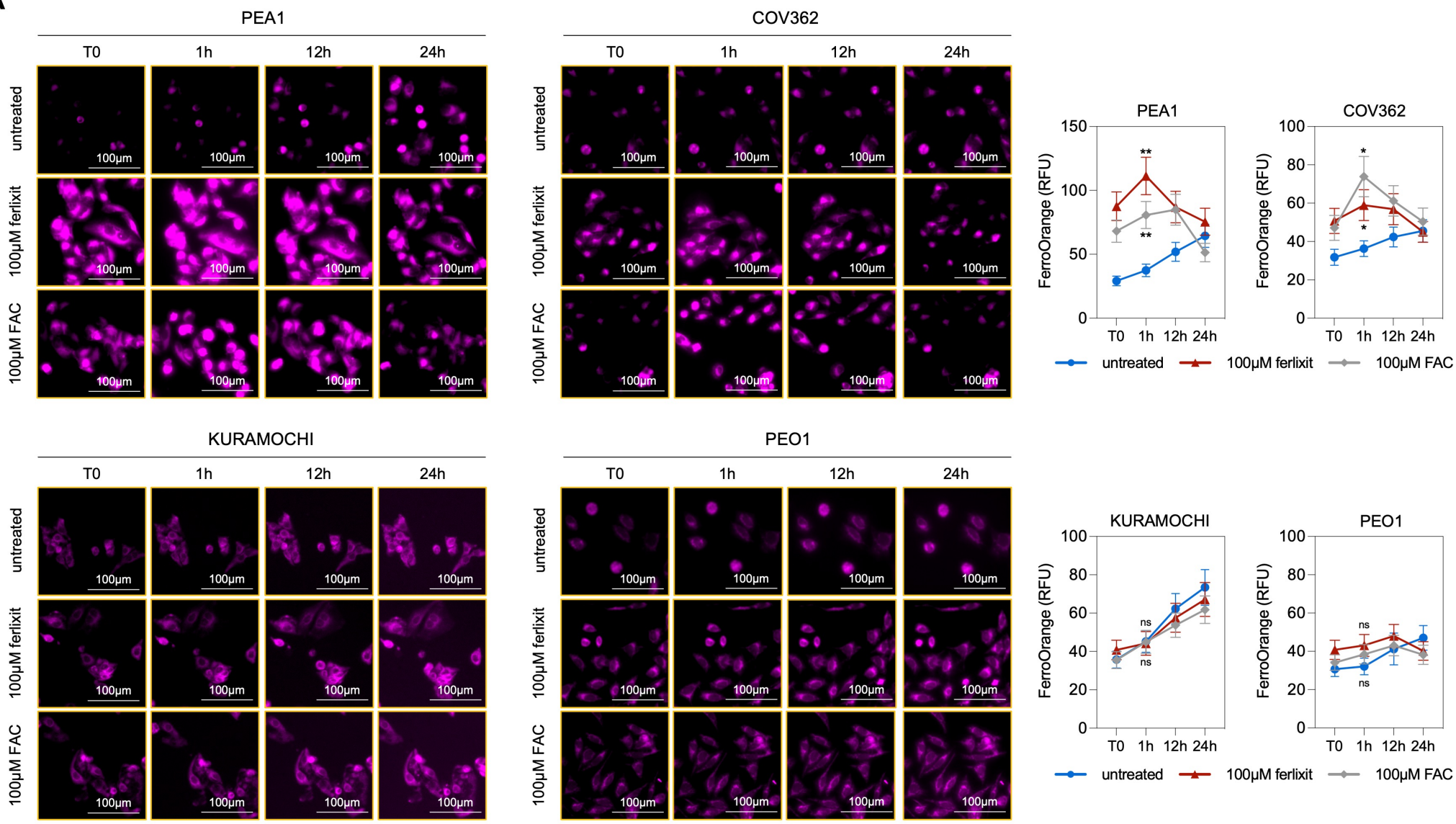
Ethics declarations

All animal procedures were approved by the Italian Ministry of Health (Authorization No. 683/2024-PR) and were performed at the Department of Molecular Medicine and Medical Biotechnology, University of Naples Federico II, in accordance with Italian regulations governing animal experimentation and in compliance with the principles of the Declaration of Helsinki. This study did not involve human participants, human data, or human tissue.

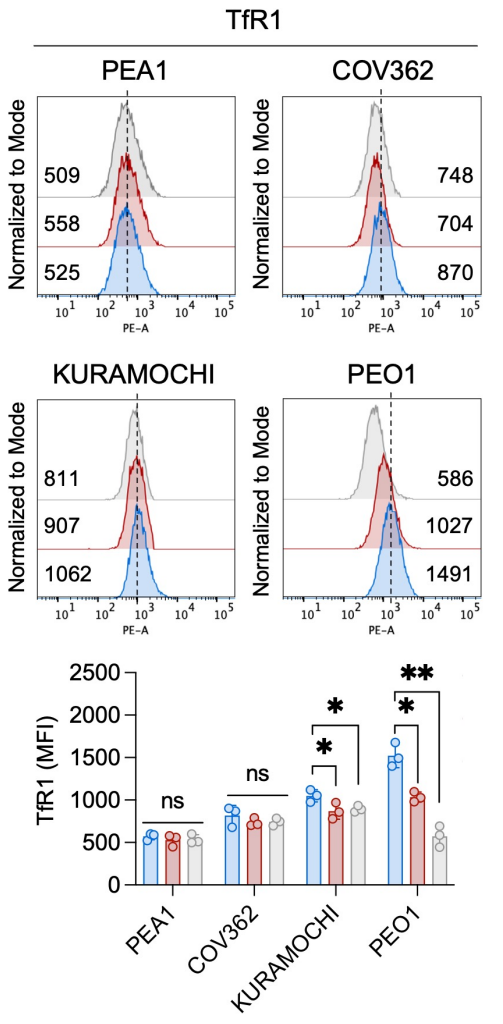

A
Cell viability (%)
PEA1
COV362
KURAMOCHI
PEO1
IHOSE
ferlixit
[μM] 0 25 50 100 250 500
FAC
B
untreated
100μM ferlixit (24h)
100μM FAC (24h)
200μm
% Red Nuclei norm (RFU)
ns
Hoechst 33342
Dead cells
C
PI+ cells (%)
Fer-1
Z-VAD
Necr-1
Baf
D
% Ballooned cells
Ballooning phenotype


A
untreated
100µM ferlixit (24h)
100µM FAC (24h)
PEA1
COV362
KURAMOCHI
PEO1
IHOSE
200µm
% ROS norm (RFU)
Hoechst 33342
PhenoVue™ ROS 670
untreated
100µM ferlixit (24h)
100µM FAC (24h)
B
PE-A
Alexa Flour 488-A
BODIPY-C11 (MFI)
0,12
36,7
13,9
0,049
20,1
8,12
0,33
2,09
1,08
0,017
0,48
0,14
1,67
3,03
1,68
C
22kDa
36kDa
GPX4
GAPDH
GPX4 optical densitometry

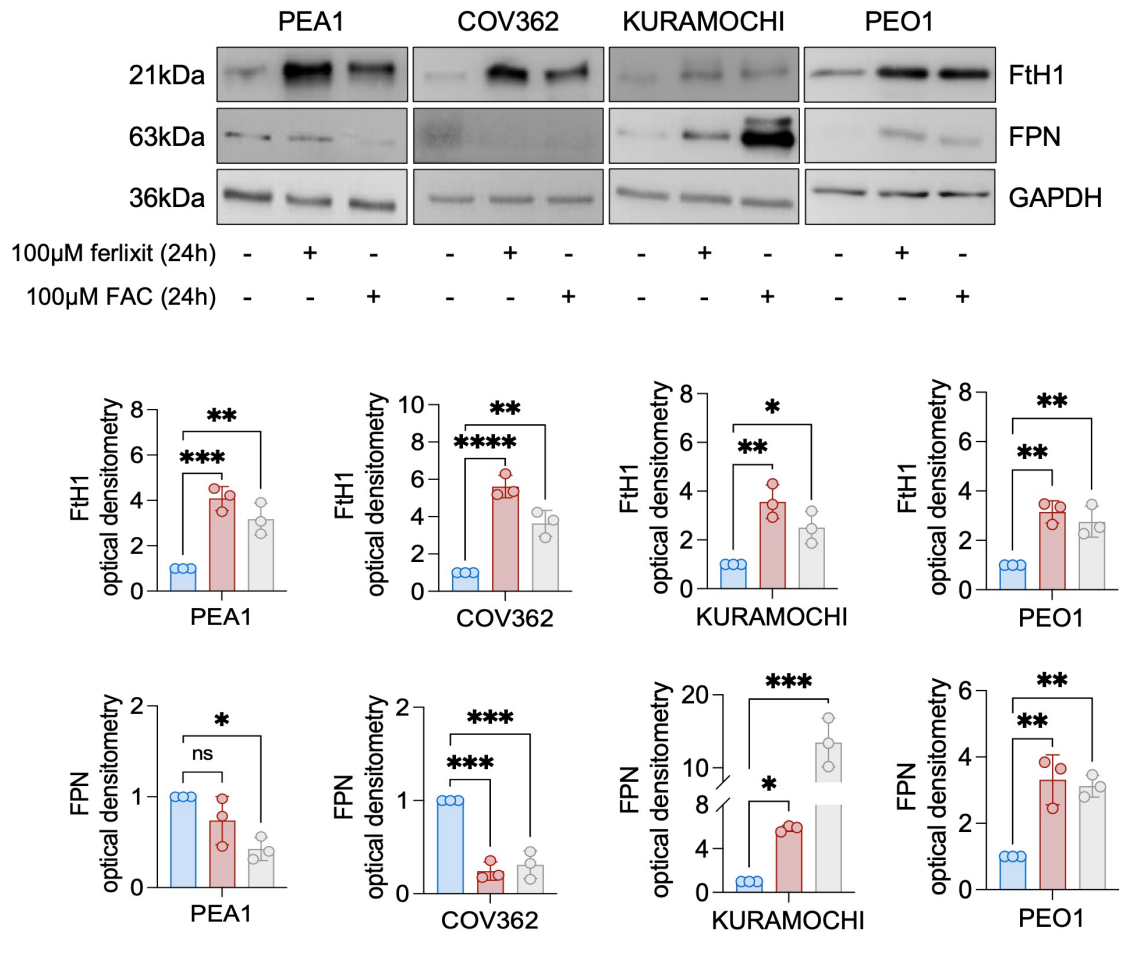
A

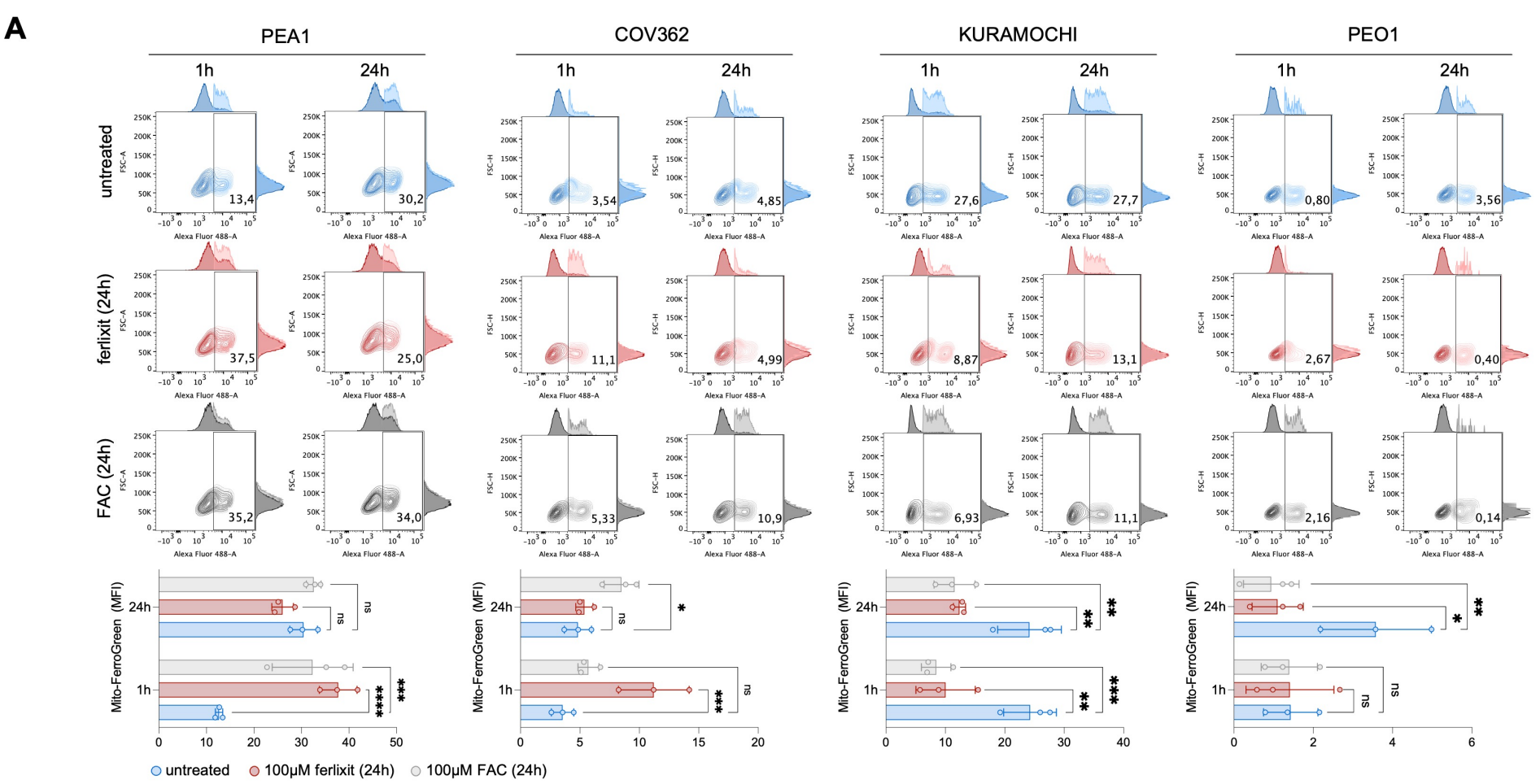

PEA1
COV362
KURAMOCHI
PEO1
T0
1h
12h
24h
untreated
100μM ferlixit
100μM FAC
100μm
FerroOrange (RFU)
untreated
100μM ferlixit
100μM FAC

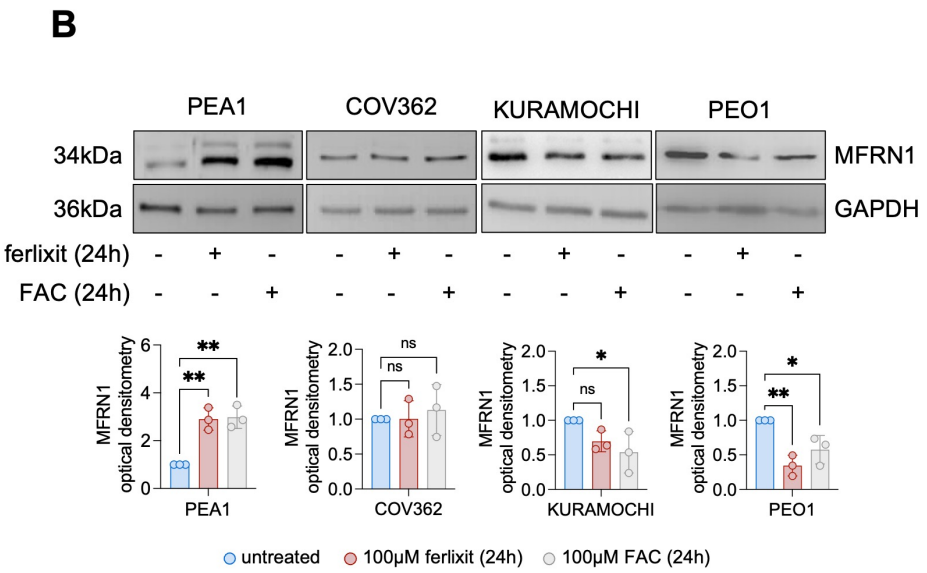
B

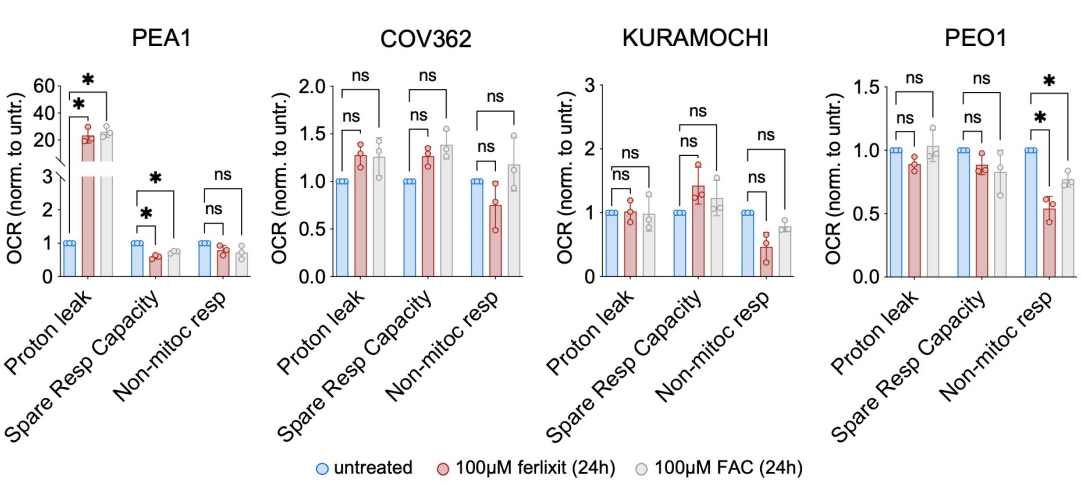

TfR1
PEA1
COV362
KURAMOCHI
PEO1
Normalized to Mode
509
558
525
748
704
870
811
907
1062
586
1027
1491
PE-A
TfR1 (MFI)
ns
untreated
100μM ferlixit (24h)
100μM FAC (24h)

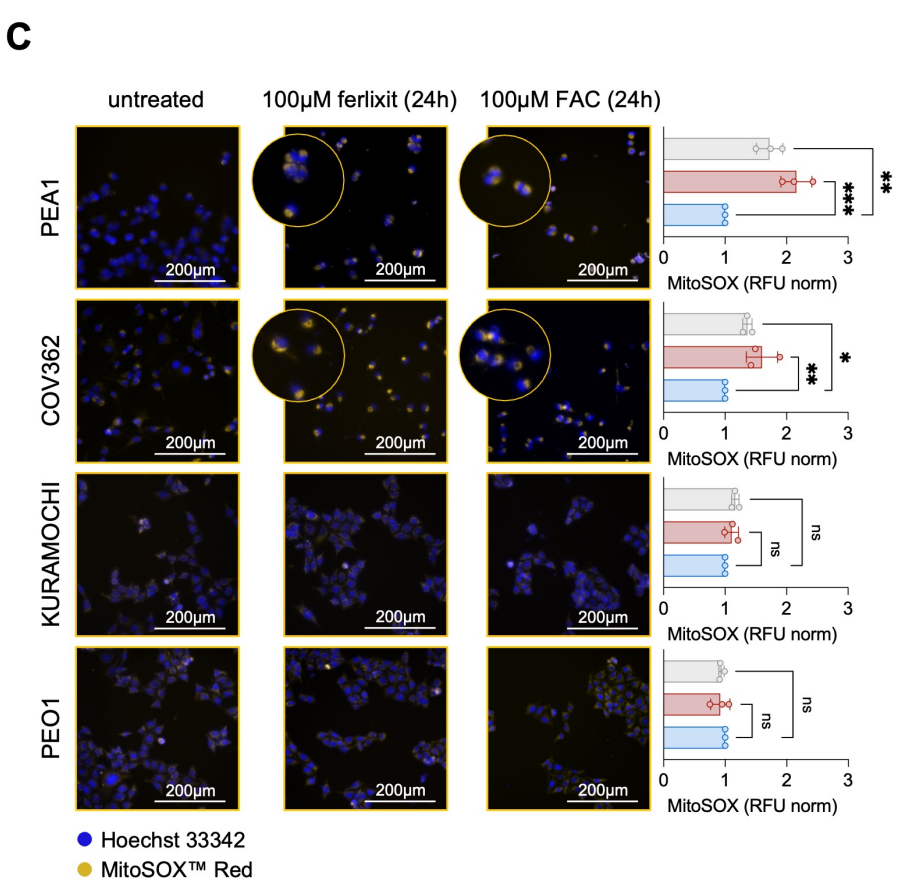
C

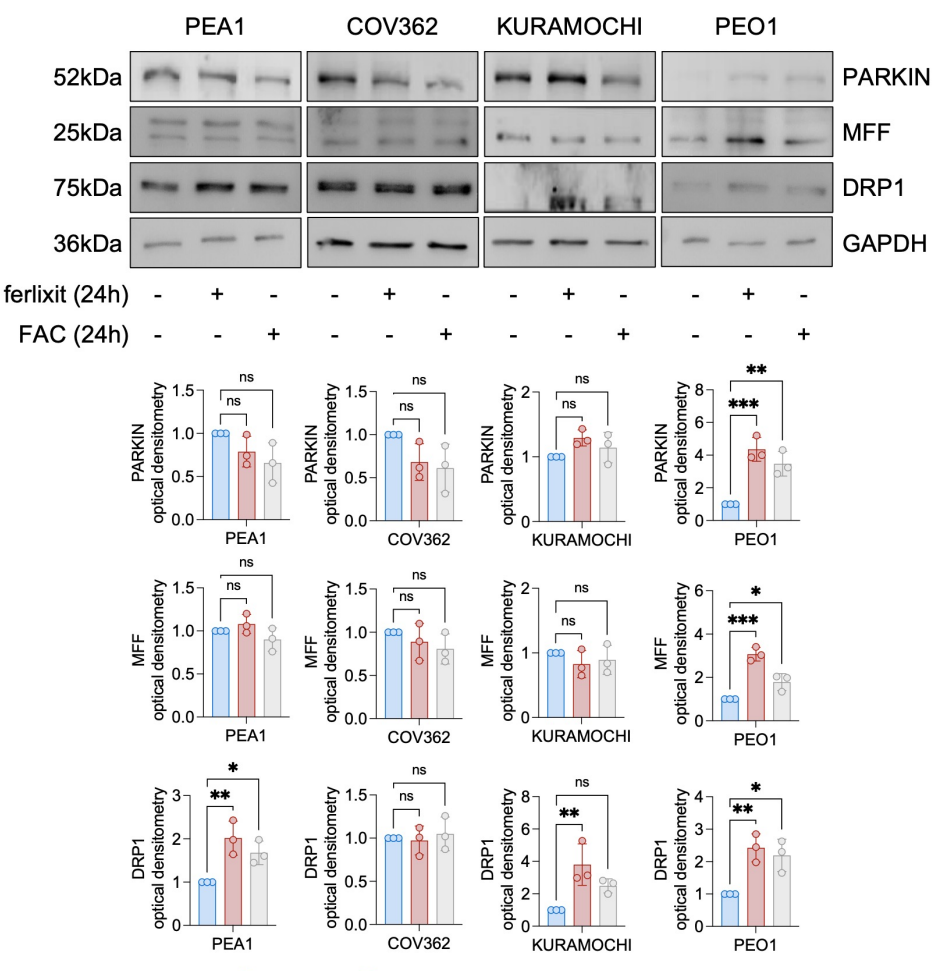

PEA1
COV362
KURAMOCHI
PEO1
21kDa
63kDa
36kDa
FtH1
FPN
GAPDH
100μM ferlixit (24h)
100μM FAC (24h)
FtH1 optical densitometry
FPN optical densitometry
untreated
100μM ferlixit (24h)
100μM FAC (24h)

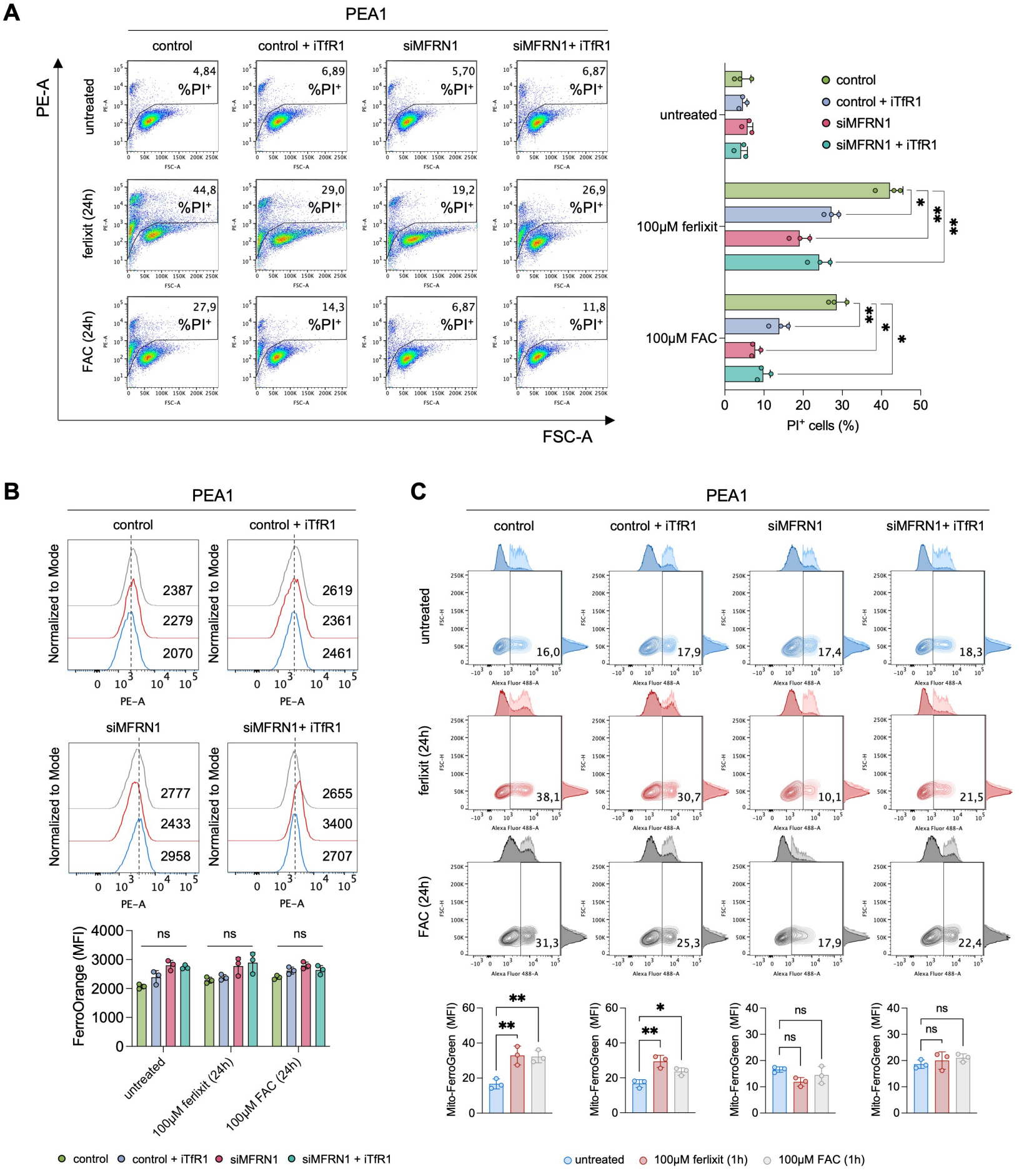

A
PEA1
COV362
KURAMOCHI
PEO1
1h
24h
untreated
ferlixit (24h)
FAC (24h)
FSC-A
FSC-H
Alexa Fluor 488-A
13,4
30,2
3,54
4,85
27,6
27,7
0,80
3,56
37,5
25,0
11,1
4,99
8,87
13,1
2,67
0,40
35,2
34,0
5,33
10,9
6,93
11,1
2,16
0,14
Mito-FerroGreen (MFI)
ns
*
**
***
****
untreated
100μM ferlixit (24h)
100μM FAC (24h)

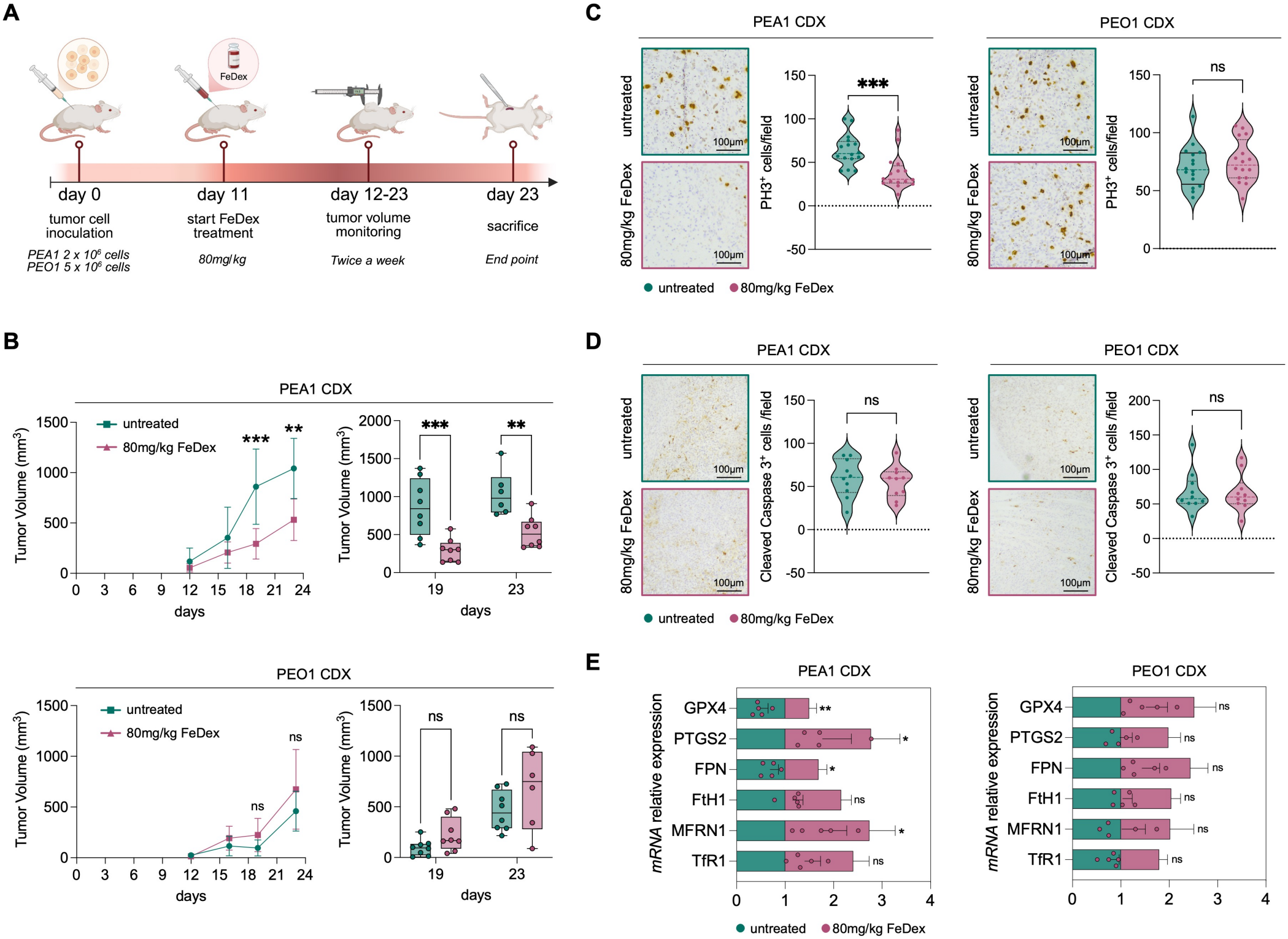

B
PEA1
COV362
KURAMOCHI
PEO1
34kDa
36kDa
MFRN1
GAPDH
ferlixit (24h)
FAC (24h)
MFRN1 optical densitometry
untreated
100μM ferlixit (24h)
100μM FAC (24h)


D
PEA1
COV362
KURAMOCHI
PEO1
OCR (norm. to untr.)
Proton leak
Spare Resp Capacity
Non-mitoc resp
untreated
100μM ferlixit (24h)
100μM FAC (24h)


C
untreated
100μM ferlixit (24h)
100μM FAC (24h)
PEA1
COV362
KURAMOCHI
PEO1
200μm
MitoSOX (RFU norm)
Hoechst 33342
MitoSOX™ Red


E
PEA1
COV362
KURAMOCHI
PEO1
52kDa
25kDa
75kDa
36kDa
PARKIN
MFF
DRP1
GAPDH
ferlixit (24h)
FAC (24h)
optical densitometry
untreated
100μM ferlixit (24h)
100μM FAC (24h)


A
PEA1
control
control + iTfR1
siMFRN1
siMFRN1+ iTfR1
untreated
ferlixit (24h)
FAC (24h)
4,84 %PI+
6,89 %PI+
5,70 %PI+
6,87 %PI+
44,8 %PI+
29,0 %PI+
19,2 %PI+
26,9 %PI+
27,9 %PI+
14,3 %PI+
6,87 %PI+
11,8 %PI+
PE-A
FSC-A
100µM ferlixit
100µM FAC
PI+ cells (%)
B
PEA1
Normalized to Mode
2387
2279
2070
2619
2361
2461
2777
2433
2958
2655
3400
2707
FerroOrange (MFI)
ns
untreated
100µM ferlixit (24h)
100µM FAC (24h)
C
PEA1
16,0
17,9
17,4
18,3
38,1
30,7
10,1
21,5
31,3
25,3
17,9
22,4
Alexa Fluor 488-A
Mito-FerroGreen (MFI)
100µM ferlixit (1h)
100µM FAC (1h)


A
FeDex
day 0
tumor cell inoculation
PEA1 2 x 10⁶ cells
PEO1 5 x 10⁶ cells
day 11
start FeDex treatment
80mg/kg
day 12-23
tumor volume monitoring
Twice a week
day 23
sacrifice
End point
B
PEA1 CDX
untreated
80mg/kg FeDex
Tumor Volume (mm³)
days
***
**
PEO1 CDX
ns
C
PEA1 CDX
PEO1 CDX
untreated
80mg/kg FeDex
100μm
PH3⁺ cells/field
***
ns
D
Cleaved Caspase 3⁺ cells /field
E
mRNA relative expression
GPX4
PTGS2
FPN
FtH1
MFRN1
TfR1

Supplementary Files

This is a list of supplementary files associated with this preprint. Click to download.

- UncroppedImmunoblotGiorgioetal.pdf
- UncroppedImmunoblotGiorgioetal.pdf
- UncroppedImmunoblotGiorgioetal.pdf
- SupplementaryMaterialGiorgioetal.pdf
- SupplementaryMaterialGiorgioetal.pdf
- SupplementaryMaterialGiorgioetal.pdf